Physics of Fluids ARTICLE scitation.org/journal/phf

Aeroacoustic analysis of the tip-leakage flow of an ultrahigh bypass ratio fan stage

Cite as: Phys. Fluids **35**, 047104 (2023); doi: 10.1063/5.0146143
Submitted: 10 February 2023 · Accepted: 18 March 2023 ·
Published Online: 4 April 2023

Jean Al-Am,[1,2,a)] Vincent Clair,[1] Alexis Giauque,[1] Jérôme Boudet,[1] and Fernando Gea-Aguilera[2]

AFFILIATIONS

[1]Univ Lyon, École Centrale de Lyon, INSA Lyon, Université Claude Bernard Lyon I, CNRS, Laboratoire de Mécanique des Fluides et d'Acoustique, UMR 5509, 36 Avenue Guy de Collongue, F-69134 Ecully, France
[2]Safran Aircraft Engines, 77550 Moissy-Cramayel, France

[a)]Author to whom correspondence should be addressed: jean.al-am@ec-lyon.fr

ABSTRACT

A detailed aeroacoustic analysis of the flow induced by the clearance between the fan tip and the shroud is performed in a scale-model fan stage of an ultrahigh bypass ratio turbofan engine, which was designed to operate at transonic regimes. A wall-modeled large eddy simulation is performed at approach condition, which corresponds to a fully subsonic operating point. The contributions of the tip-gap noise to the total fan noise are investigated using the Ffowcs Williams and Hawkings analogy. The surface is split into two parts: the tip region and the rest of the blade in order to analyze the acoustic contributions of these two regions separately. It is shown that the tip-gap region generates a significant noise component above 2 kHz, which corresponds to approximately 1.2 times the blade passing frequency. Two separate tip-leakage vortices are identified in the vicinity of the fan tip. The dominant noise sources in the tip-gap region are observed at the trailing edge of the fan blade. The wall pressure spectra in the tip-gap region and the coherence of pressure fluctuations between monitor points at different positions show an acoustic contribution of the tip-leakage flow at two different frequency ranges. The first range corresponds to medium frequencies between 2 and 9 kHz, and the second range corresponds to high frequencies between 10 and 25 kHz. The analysis of dynamic mode tracking, fluctuating pressure and velocity spectra, and instantaneous flow fields relates specific vortices in the tip-gap flow to their spectral signature and paves the way for further analytical modeling of tip-gap noise sources.

I. INTRODUCTION

In the next generation of ultrahigh bypass ratio (UHBR) aero-engines, the fan noise contribution to the aircraft noise is expected to increase during takeoff and landing.[1,2] The rotor self-noise is a significant noise source in UHBR aero-engines due to an increased fan diameter and a reduced nacelle length. The rotor self-noise sources include the trailing edge noise, the separation noise, and the tip-gap noise. Trailing edge noise is generated by the diffraction of the turbulent boundary layers near the trailing edge.[3] The separation noise may occur at partial operating points and is due to an increased angle of attack that leads to large pressure fluctuations close to the leading edge of the rotor blade.[4] The tip-gap noise is related to the leakage flow in the fan clearance and will be studied in detail in this paper.

A radial clearance between the fan tip and the shroud is necessary to avoid any contact between the rotor blades and the outer casing, as shown in Fig. 1(a). The fan clearance leads to the development of a highly turbulent and three-dimensional unsteady secondary flow, due to the pressure difference between the pressure and suction sides of the rotor blade in the tip region. This complex flow can increase aerodynamic losses and noise emissions.

Initial studies on the tip-leakage flow performed by Rains[5] have shown that the flow at the blade tip is perpendicular to the camber line, when passing from the pressure side to the suction side. This leakage flow is rolled up when interacting with the main flow, which leads to the formation of a tip-leakage vortex (TLV). The TLV is characterized by highly vortical structures,[6] which may interact with the trailing edge of the rotor blades and with the mainstream flow, and strong unsteady mechanisms. This leads to a reduction in the aerodynamic performance of the fan[6,7] and increased far-field noise emissions.[8]

Many experimental[9,10] and numerical[11–14] studies have been performed on isolated airfoil configurations to analyze the characteristics of the tip-leakage flow, without the additional aerodynamic mechanisms and fan noise sources that appear in a rotating configuration. A parametric study has been performed by Grilliat *et al.*[9] on a NACA 5510 airfoil placed between two side plates, including the effects of the flow speed, the angle of attack, and the tip-gap size (varying from 1%

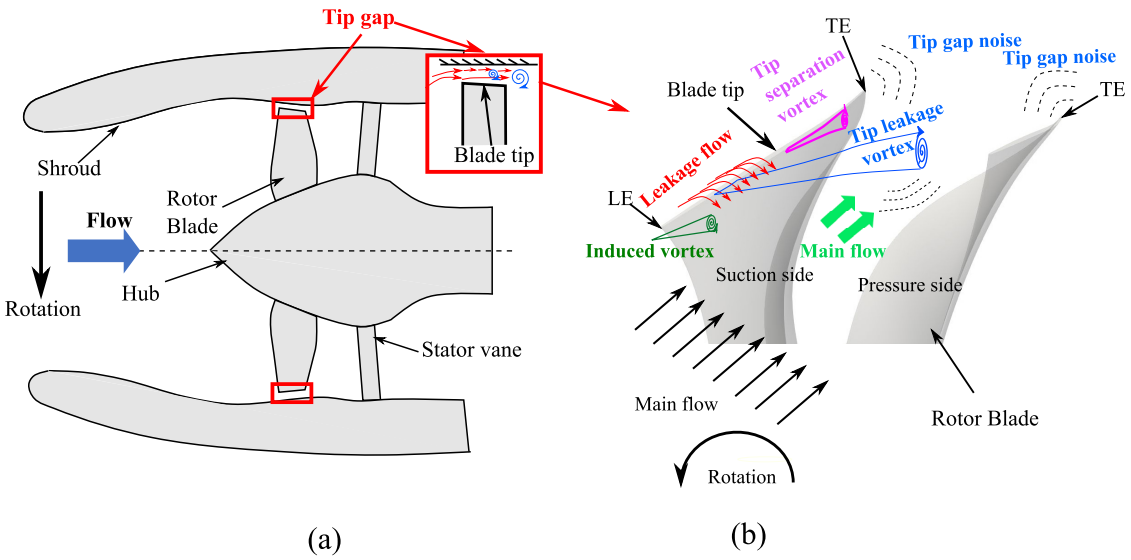

FIG. 1. (a) Fan/OGV stage. (b) Different flow structures in the tip gap region. "LE" refers to the leading edge. "TE" refers to the trailing edge.

to 12% of the rotor span) on the topology of the tip-leakage flow and the noise emissions. The flow speed has shown little effect on the tip-leakage flow topology, whereas a significant influence of the angle of attack and the tip-gap size was found. Two main noise sources were identified in the far-field acoustic spectrum. The first noise source, which has been identified at frequencies ranging from 0.7 to 3.5 kHz, has a dipolar radiation pattern and corresponds to turbulent structures generated by the flow separation in the tip-gap region that are convected past the trailing edge. The second noise source, which dominates at frequencies ranging from 4 to 7 kHz, has a quadrupolar radiation pattern and is associated with vortices in the shear layers of the tip-leakage flow. Additionally, different numerical approaches, such as large eddy simulation (LES),[14] zonal LES,[11] and lattice Boltzmann method,[15] have shown that the main noise source at the airfoil tip is located between the mid-chord and the trailing edge for different flow conditions. The main contribution of the tip-gap noise was observed between 2 and 6 kHz.

To investigate more representative turbomachinery configurations, several studies have focused on rectilinear compressor cascades. Experimental studies performed by Kang and Hirsh[16] over a cascade of seven NACA 65-1810 airfoils, with varying tip-gap size, found three types of tip vortices: (i) a TLV formed close to the leading edge, (ii) a tip separation vortex (TSV) formed along the pressure side of the airfoil tip and leaving the clearance near the mid-chord, and (iii) a secondary vortex developed at the suction side of the airfoil tip, which interacts with the TSV. An induced vortex (IV) can also be found alongside the TLV and rotating in the opposite direction.[6,11] The different types of tip vortices are presented in Fig. 1(b). Several numerical simulations[6,17,18] have also been performed on the same linear compressor cascade with a tip clearance. You *et al.*[6] performed incompressible LES on the rectilinear compressor cascade with a moving end wall. The TLV was found in a region of significant streamwise and pitchwise vorticity magnitudes. The viscous losses in the cascade end wall region were mainly associated with the spanwise and pitchwise velocity gradients. To study both the tip-leakage flow topology and the noise sources, Koch *et al.*[17,18] performed a wall-resolved compressible LES on the rectilinear compressor cascade. The main tip noise mechanisms were identified through an aeroacoustic analysis using the Ffowcs Williams and Hawkings (FWH) analogy,[19] and a dynamic mode decomposition technique. The main noise sources were found at approximately 75% of the chord length and at frequencies between 5 and 6 kHz.

To investigate realistic turbomachinery configurations, including the effects of the fan rotation, several experimental[20,21] and numerical[7,22,23] studies have been performed using a scale model fan stage, which is known as the NASA source diagnostic test (SDT) configuration. Experimental comparisons between the noise levels from the fan/outlet guide vanes (OGV) configuration and the fan-only configuration (without OGV) have been useful to separate the contributions of the main noise sources, such as the rotor–stator interaction and the tip-leakage noise.[1] The contribution of the tip-leakage noise source appears to be dominant below 6 kHz. Additionally, a comparison of the tip flow topology and the noise at approach and cutback operating conditions has been performed by Kholodov *et al.*[23] using LES. A stronger TLV with a smaller deviation angle with respect to the fan blades was observed at cutback condition when compared with approach condition.

Both the tip-leakage flow topology and the tip-gap noise have been extensively studied on simplified configurations. However, the aeroacoustic analyses of the tip-leakage flow in a realistic fan stage are still limited. Additionally, the tip-gap noise in modern fan stages, which are designed to operate at transonic conditions, has not been addressed yet. The objective of the present study is to investigate the tip-leakage flow and the noise emissions from a state-of-the-art fan/OGV stage of a scale model UHBR aero-engine, using wall-modeled (WM) LES. Although the fan blade has been designed to operate at a transonic tip speed, a fully subsonic operating point, which corresponds to an acoustic certification point at approach condition,

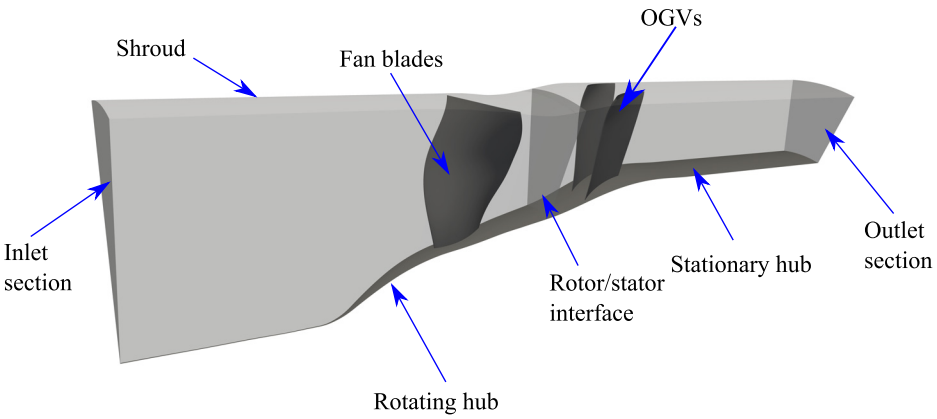

FIG. 2. Computational domain of the ECL5 fan/OGV stage.

has been adopted in the present study. A suitable LES setup has been chosen to solve the turbulent eddies in the boundary layers and wakes and perform a direct noise prediction in the fan stage. To reduce the computational cost, only a periodic angular sector of the fan stage without core flow is considered here, which includes one fan blade and two OGVs in the computational domain. The tip-leakage flow is analyzed using steady and unsteady flow characteristics in the tip region of the fan. The relative contribution of the different tip-gap noise mechanisms to the overall noise level is investigated using a coherence analysis, the FWH analogy[19] from the solid surface of the fan blade, and a dynamic mode tracking (DMT) technique.

This paper is organized as follows: Section II presents a description of the numerical setup, which includes the computational domain, the mesh properties, and the LES numerical parameters. The aerodynamic results and the flow topology in the tip-gap region are presented in Sec. III. The main noise sources in the fan tip region and the contributions of the tip-gap noise to the far-field noise are then analyzed in Sec. IV. Finally, the main findings and possible extensions to the present work are listed in Sec. V.

II. NUMERICAL SETUP

A. Computational domain and operating conditions

In the present work, LES are performed using the state-of-the-art ECL5 fan/OGV stage,[24] which has been conceived at École Centrale de Lyon. This fan stage is composed of 16 rotor blades and 31 stator vanes and has been designed according to technical requirements for a mid-range commercial aircraft. The original vane count is adapted to 32 vanes to allow for a $2\pi/16$ periodicity. This geometry modification is performed by keeping the solidity fixed, which is defined as the ratio between the chord length and the inter-vane spacing.[25] The ECL5 configuration has also been investigated in a previous study by the authors[26] using a similar numerical setup.

An overview of the computational domain is shown in Fig. 2. The domain extends from $3.75c_r$ upstream of the fan to $4.25c_s$ downstream of the stator, where c_r and c_s are the rotor and stator mid-span chord lengths, respectively. In the present study, the LES are performed at approach condition with a rotational speed of $\Omega = 6050$ rpm, which corresponds to 55% of the nominal fan speed. The reference mass flow rate at approach condition is $\dot{m} = 20$ kg/s. Using this mass flow rate, a large recirculation bubble may appear on the suction side of the fan, near the leading edge, which leads to a significant noise signature.[4] Thus, a larger mass flow rate ($\dot{m} = 21.7$ kg/s) is chosen for the present study in order to reduce the size of the recirculation bubble and to minimize its impact on the fan noise.[4] At these conditions, the fan operates in a fully subsonic regime and the Reynolds number based on the chord length is approximately 10^6.

The fan airfoil sections at different radial locations are presented in Fig. 3. The hub corresponds to a spanwise position of 0% and the fan tip to 100%. The design of these airfoil sections is based on the flow conditions at the design speed ($\Omega_n = 11\,000$ rpm). Highly cambered airfoils are located near the hub, where the flow is subsonic. For airfoils at higher spanwise positions, the camber is reduced. This is due to the flow features at design speed near the fan tip, where the flow speed is transonic and the pressure gradient is highly influenced by the presence of shock waves. This had an influence on the blade design close to the casing. Particularly, the airfoil section at the fan tip is relatively flat near the leading edge, and the axial location of the maximum camber is set to $0.7c_r$. These properties are typical of airfoils operating at transonic speeds and are expected to have a significant effect on the flow topology in the tip gap region.

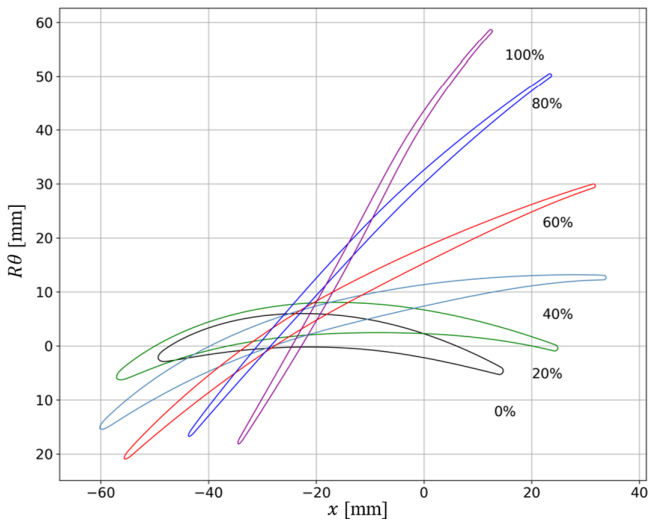

FIG. 3. Rotor profiles for different heights.

B. Numerical parameters

In the present work, the LES governing equations are solved using the AVBP code, which is an explicit unstructured compressible LES solver that has been developed by CERFACS.[27] Two LES domains are coupled by using the CWIPI library developed by ONERA.[28] The first domain corresponds to the rotating domain that contains one fan blade, and the second domain corresponds to the stationary domain that contains two stator vanes.

The two-step Taylor–Galerkin convection (TTGC) scheme[29] is used to solve the filtered Navier–Stokes equations in space and time. The TTGC scheme[29] is an explicit third-order finite volume convective numerical scheme. The SIGMA subgrid-scale model[30] is used to model the unresolved turbulent eddies. At the inlet and outlet sections of the domain, nonreflecting Navier–Stokes characteristic boundary conditions (NSCBC)[31] are used. At the inlet section, a uniform mean flow is injected in the axial direction along with a total pressure of $P_0 = 101\,325$ Pa and total temperature of $T_0 = 300$ K. At the outlet section, the static pressure is adjusted to obtain the desired mass flow rate. On the azimuthal boundaries of the computational domain, periodic boundary conditions are used. On the wall surfaces, including the blade, vanes, shroud, and hub, a no-slip boundary condition is used. The inner part of the boundary layers is modeled using a wall law,[32] with a dimensionless velocity relative to the wall $u^+ = \frac{1}{\kappa}\ln(Ay^+)$ for $y^+ > 11.45$, with $\kappa = 0.41$ and $A = 9.2$. Below $y^+ = 11.45$, a linear law is imposed. The time step for the simulation is set to $\Delta t = 2.8 \times 10^{-8}$ s and the computational cost is approximately 105×10^3 CPUh per rotation. Numerical and statistical convergences are studied. Numerical convergence corresponds to the end of the transient state, whereas statistical convergence corresponds to the convergence of the flow statistics. Based on a convergence analysis methodology introduced by Boudet *et al.*,[33] about three full fan rotations, i.e., 3×16 blade passages, are performed for the convergence, and four additional fan rotations are performed for the sampling, which includes flow statistics and acoustics.

C. Mesh characteristics

An overview of the mesh in the fan tip region is presented in Fig. 4. The unstructured hybrid mesh is composed of several types of elements. Prismatic cells are used on the walls, tetrahedral cells are used away from the walls, and pyramidal cells are used in the transition regions between prismatic and tetrahedral cells.

In the prismatic mesh region, the first layer at the wall has the smallest spacing and is characterized by the dimensionless cell sizes, x^+, y^+, and z^+ in the streamwise, transverse, and spanwise directions, respectively. The mean dimensionless cell sizes are set to $x^+ = z^+ = 125$ and $y^+ = 25$. The cell size is progressively increased away from the walls using an expansion ratio of 1.1 in the present LES. The total number of prismatic layers in the mesh refinement regions close to the walls is set to 14.

In order to ensure an adequate resolution of the turbulence in the wakes and to propagate the acoustic waves in the fan stage, the LES mesh is designed according to turbulent and acoustic criteria.[34] For an accurate description of the turbulent eddies in the wake regions, the mesh size is smaller than 30 times the Taylor micro-scale, $\lambda_{Ta} = (10\frac{\nu k_t}{\epsilon})^{1/2}$, where ν is the kinematic viscosity, k_t is the turbulent kinetic energy, and ϵ is the turbulent dissipation rate. Additionally,

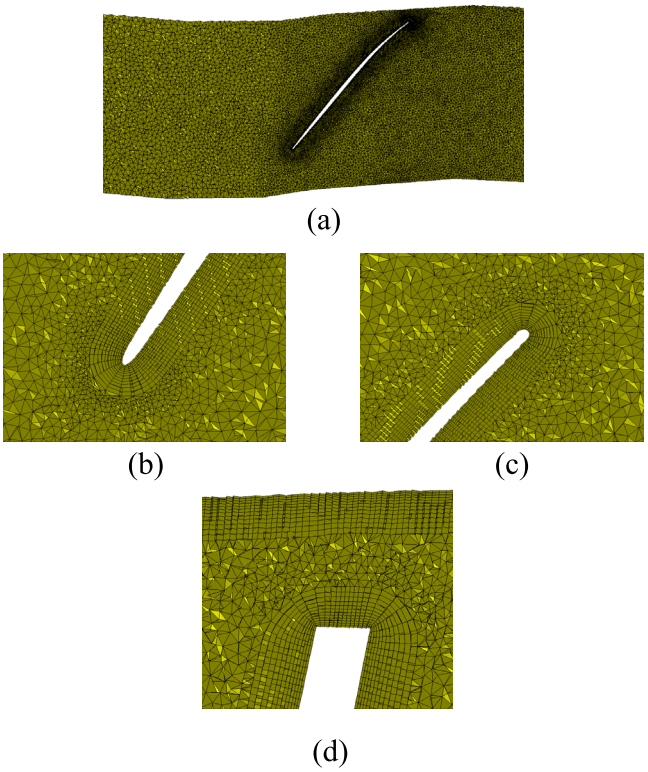

FIG. 4. (a) Mesh around the rotor blade at 95% of the span. Mesh refinements near the rotor leading edge (b), the rotor trailing edge (c), and in the rotor tip-clearance region (d).

for a correct propagation of the acoustic waves below a chosen cutoff frequency, 13 points per acoustic wavelength are required. In this study, the mesh cutoff frequency is set to $f_c = 20$ kHz, and the acoustic wavelength is defined as $\lambda_{ac} = \frac{c_0(1-M)}{f_c}$, where c_0 is the speed of sound and M corresponds to the Mach number.

In the tip clearance region, 26 prismatic layers and eight tetrahedral cells are imposed in the radial direction, as shown in Fig. 4(d).

III. AERODYNAMICS

A. Tip flow topology

The distribution of isentropic Mach number, M_{is}, which is related to the static pressure distribution on the fan blade, is presented in Fig. 5 at three spanwise positions. Similar trends in the M_{is} distribution can be observed at $H = 50\%$ and 80% of the rotor span, where the aerodynamic loading is higher close to the leading edge. However, the shape of M_{is} distribution between these two positions ($H = 50\%$ and $H = 80\%$) is different close to the leading edge, where a plateau of M_{is} at $H = 80\%$ indicates the presence of a small recirculation bubble. When comparing the different spanwise positions, it can be seen that as the radius increases, the blade loading is shifted toward the trailing edge. The loading distribution at $H = 98\%$, which corresponds to a spanwise position close to the fan tip region, is significantly different. Between the leading edge and $0.5c_r$, the pressure jump is quite small, compared to the other spanwise positions at $H = 50\%$ and $H = 80\%$. From approximately $0.6c_r$, a significant increase in the pressure

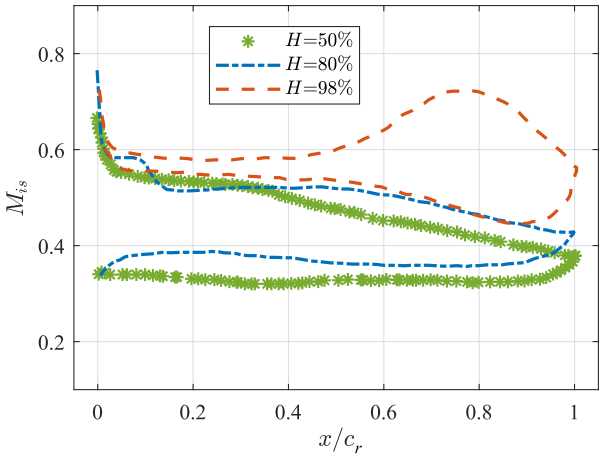

FIG. 5. Averaged isentropic Mach number M_{is} along the rotor blade, for different spanwise positions H.

difference between the pressure and suction sides of the blade is observed. This behavior can be associated with the blade shape that was designed to operate at a transonic speed near the fan tip and generate loading through the presence of shock waves. However, the operating point in the present LES simulation corresponds to a fully subsonic regime at approach condition. It should be noted that the tip blade section presents a particular camber evolution. Between the leading edge and the maximum camber position, the airfoil is relatively flat and thin, and the position of the maximum camber is located at $0.7c_r$, which is unusual for subsonic airfoils.

The flow structures in the tip-gap region are shown in Figs. 6 and 7 using averaged and instantaneous iso-surfaces of the Q-criterion, respectively. The tip flow structures are colored by the normalized helicity *Hel*, which is defined as

$$Hel = \frac{\vec{\Omega_v} \cdot \vec{u}}{||\vec{\Omega_v}|| \cdot ||\vec{u}||}, \quad (1)$$

where $\vec{\Omega_v}$ and $\vec{u}$ are the relative vorticity and velocity vectors, respectively. The helicity indicates the direction of rotation of a vortex; a positive value of helicity means that the vortex rotates in the clockwise

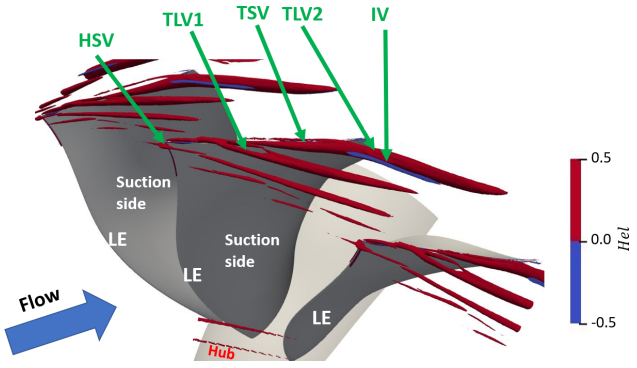

FIG. 6. Averaged iso-surface of Q-criterion ($Qc_r^2/U_0^2 = 500$), where U_0 is the free-stream velocity magnitude) in the tip-gap region, colored by the normalized helicity.

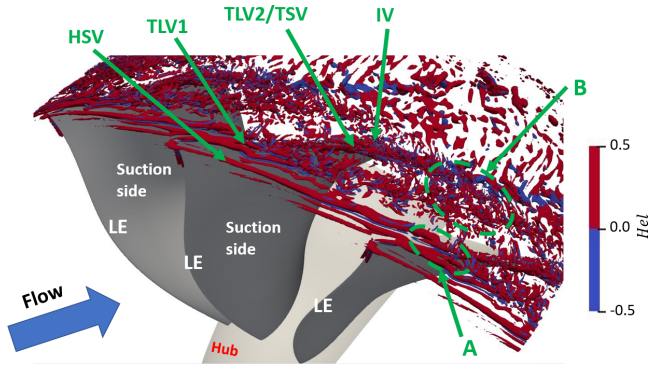

FIG. 7. Instantaneous iso-surface of Q-criterion ($Qc_r^2/U_0^2 = 500$) in the tip-gap region, colored by the normalized helicity.

direction with respect to the flow from the fan front view, and a negative value means that the vortex rotates in the counterclockwise direction. Several vortical structures are observed in the tip-gap region. A first tip-leakage vortex, which is referred to as "TLV1" in Figs. 6 and 7, is formed at about $0.25c_r$ due to the roll up of the tip-leakage jet coming from the pressure side.

A horseshoe vortex, which is referred to as "HSV" in Figs. 6 and 7, appears just upstream of the leading edge. The HSV is generated when the turbulent boundary layer on the shroud impinges the fan leading edge in a region of adverse pressure gradient.[35] The HSV generated by a blade interacts with the adjacent blade at approximately $0.25c_r$ in region "A" in Fig. 7 and seems to contribute to the TLV1.

Downstream of the TLV1, tip separation vortices, referred to as "TSV" in Figs. 6 and 7, develop on the blade tip. These vortices separate from the blade tip at about $0.7c_r$, in a region where the pressure difference between the pressure and suction sides is relatively important, as shown in Fig. 5. The formation and topology of the TLV1 and TSV in the tip-gap region have also been observed and analyzed in Fig. 10 by You *et al.*[6] and in Fig. 3 by Lamidel *et al.*[13]

Another tip-leakage vortex, referred to as "TLV2" in Figs. 6 and 7, is generated at about $0.75c_r$ due to the strong pressure difference in this region. The TLV2 is partially fed by the TLV1 coming from the adjacent fan blade. This phenomenon is known as double leakage. Additionally, an induced vortex, referred to as "IV" in Figs. 6 and 7, is observed alongside the TLV2, with an opposite direction of rotation.

After leaving the tip-gap region, the TLV1 is convected in the inter-blade passage and interacts with the other tip flow vortices. First, a TLV1 interaction occurs with the tip vortices TSV, TLV2, and IV that are generated by the same fan blade, in region "B," in Fig. 7. All the vortices are then convected in the downstream direction. Second, a part of the TLV1 moves toward the trailing edge of the adjacent blade.

The complex flow topology in the tip-gap region may be related to (i) the approach operating point and the blade tip geometry, which was designed to operate at transonic regimes, and to (ii) the tip-gap size and shape, which is larger than $0.01c_r$ and increases linearly toward the trailing edge.

To further analyze the flow topology in the tip-gap region, different values of the averaged Q-criterion are presented in Fig. 8. For the smallest value of the Q-criterion, i.e., $\bar{Q}c_r^2/U_0^2 = 500$ in Fig. 8(a), the different tip flow vortices observed in Figs. 6 and 7 can be identified.

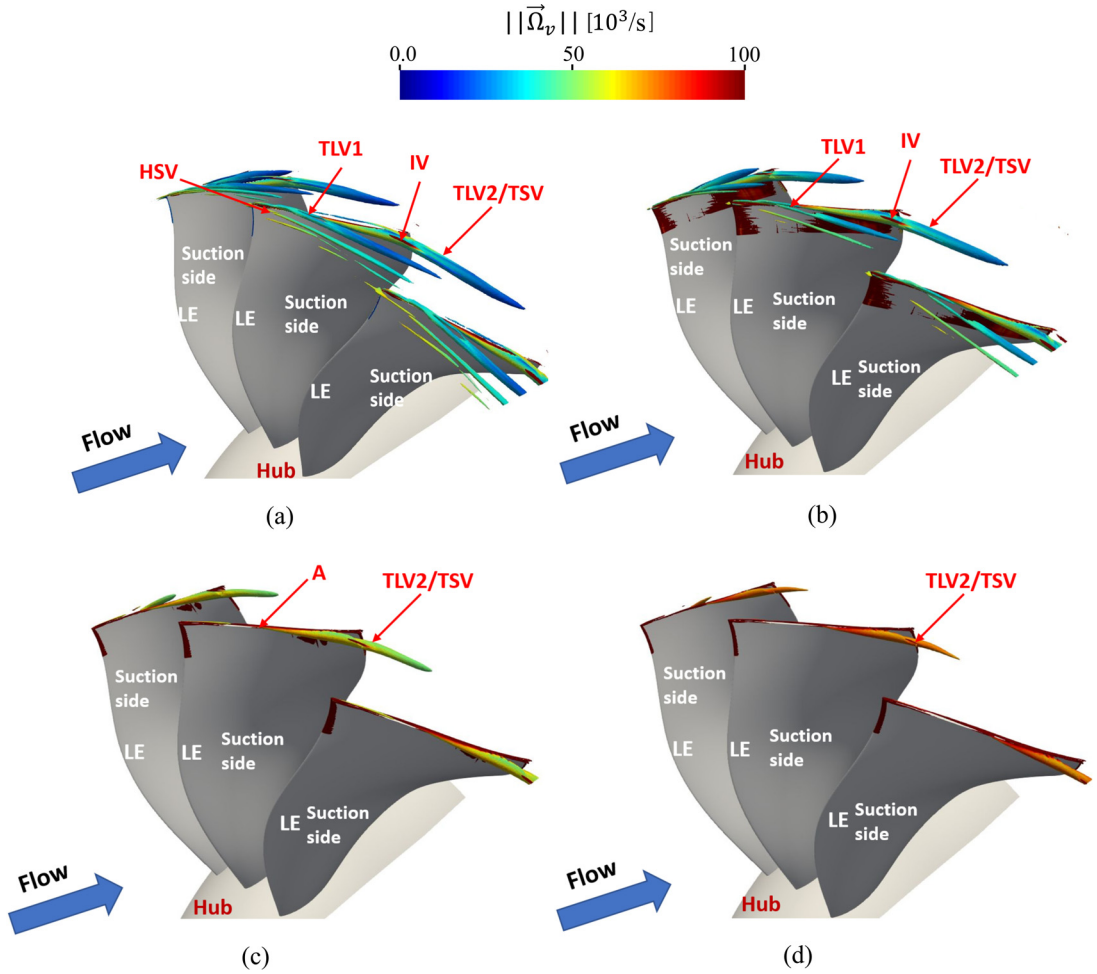

FIG. 8. Averaged Q-criterion in the tip-gap region, colored by the vorticity magnitude, for different iso-surface values: (a) $\bar{Q}c_r^2/U_0^2 = 500$, (b) $\bar{Q}c_r^2/U_0^2 = 750$, (c) $\bar{Q}c_r^2/U_0^2 = 1000$, and (d) $\bar{Q}c_r^2/U_0^2 = 1250$.

When increasing the value of the Q-criterion, less vortices can be observed. As the value of the Q-criterion increases, the rotational effect of a vortex becomes more important than its strain effect. For $\bar{Q}c_r^2/U_0^2 = 750$ in Fig. 8(b), the tip vortices TLV1, TSV, TLV2, and IV can still be identified, whereas the HSV partially disappears. Because of the relatively thin leading edge of the fan blade, particularly at the tip, the HSV formed at the leading edge is weak and can only be properly observed at small iso-surface values of the Q-criterion. For $\bar{Q}c_r^2/U_0^2 = 1000$ in Fig. 8(c), the TLV1 disappears and the tip flow separation that leads to the formation of the TSV can be clearly observed. Only the TLV2 and the TSV can be observed for $\bar{Q}c^2/U_0^2 = 1250$ in Fig. 8(d). Furthermore, as the value of the iso-surface of the Q-criterion is increased, the turbulent structures are characterized by larger vorticity magnitudes. Consequently, the rotational effect and the vorticity levels of the tip vortices TLV2 and TSV at about $0.7c_r$ are larger than those of the TLV1. This is because the tip vortices TLV2 and TSV are influenced by highly turbulent boundary layers and a stronger tip-leakage flow due to the significant pressure jump between pressure and suction sides at the fan tip.

The main characteristics of the different tip-flow vortices identified in this section are presented in Table I. "Rotation" refers to the direction of rotation of the vortex, "CW" for the clockwise direction with respect to the fan front view, and "CCW" for the counterclockwise direction. "Onset at fan tip" refers to the distance between the leading edge and the onset of the vortex in the chordwise direction of the tip blade section. "Inter-adj"/"Inter-same" indicates if there is an interaction between the vortex and the adjacent blade and the same blade, respectively. The relative intensity, in terms of vorticity magnitude, is indicated by using "+" symbols, where only one + symbol for the HSV indicates the weakest vortex.

B. Flow statistics

Figure 9 shows contours of averaged velocity components around the rotor blade at two spanwise positions, 80% and 99% of the rotor span from the hub. In the tip flow region, i.e., at 99% of the rotor span, a significant axial velocity deficit, which leads to a blockage effect, develops between two consecutive blades near the trailing edge, as

TABLE I. Summary of the main characteristics estimated for the different tip-leakage vortices.

Type of vortex	Onset at fan tip	Rotation	Relative intensity	Inter-adj	Inter-same
HSV	leading edge	CW	+	Yes	No
TLV1	$0.25c_r$	CW	++	Yes	No
TSV	$0.70c_r$	CW	++++	No	Yes
TLV2	$0.75c_r$	CW	++++	No	Yes
IV	$0.75c_r$	CCW	+++	No	Yes
Reference figure	Fig. 6	Figs. 6 and 7	Figs. 7 and 9	Figs. 6 and 7	Fig. 8

shown in Fig. 9(d). Upstream of the trailing edge, a strong increase in the axial velocity component appears close to the suction side at about $0.7c_r$, which indicates the onset of the tip vortices TSV, TLV2, and IV. Large values of the axial velocity component can also be observed in the blade passage around mid-chord, which highlights the presence of the TLV1. The blockage effect due to the tip-leakage and tip-separation vortices is also seen through a deficit of the relative circumferential velocity component (V_θ) downstream of the rotor blades. V_θ reaches large values at about $0.7c_r$, i.e., where the tip vortices TSV, TLV2, and IV appear. The radial velocity component (V_r) exhibits a pronounced variation in the region where the tip vortices TSV, TLV2, and IV appear. Radially, upward and downward flow motions can be observed in this region, which indicates a rotating tip flow. A similar behavior is observed for the TLV1 with smaller V_r values. At 80% of the rotor span, the tip-leakage vortices do not show any influence on the flow topology. At this spanwise position, large values of the axial velocity component (V_x) are observed on the suction side around mid-chord, which indicates the region of significant blade loading and is consistent with the M_{is} distribution in Fig. 5.

Figure 10 presents the three components of the root mean square (RMS) velocity fluctuations at two spanwise positions. At 80% of the rotor span, the tip flow vortices do not have any influence on the RMS velocity components. At 99% of the rotor span, a region of large RMS velocity fluctuations is observed in the inter-blade region, particularly at the axial position of the trailing edge. This corresponds to the region of axial and circumferential velocity deficits in Figs. 9(d) and 9(e). This region can be associated with the velocity fluctuations generated by the interaction of the vortices TLV1, TSV, TLV2, and IV with the main flow. The vortices generated from one blade seem to interact with the trailing edge and the wake of the adjacent blade. The velocity fluctuations from the tip vortices are significantly larger than those in the blade boundary layers and wakes.

The three components of the RMS velocity fluctuations are also presented at an axial cross section downstream of the rotor trailing edge, in Fig. 11. Significant levels of RMS velocity fluctuations are

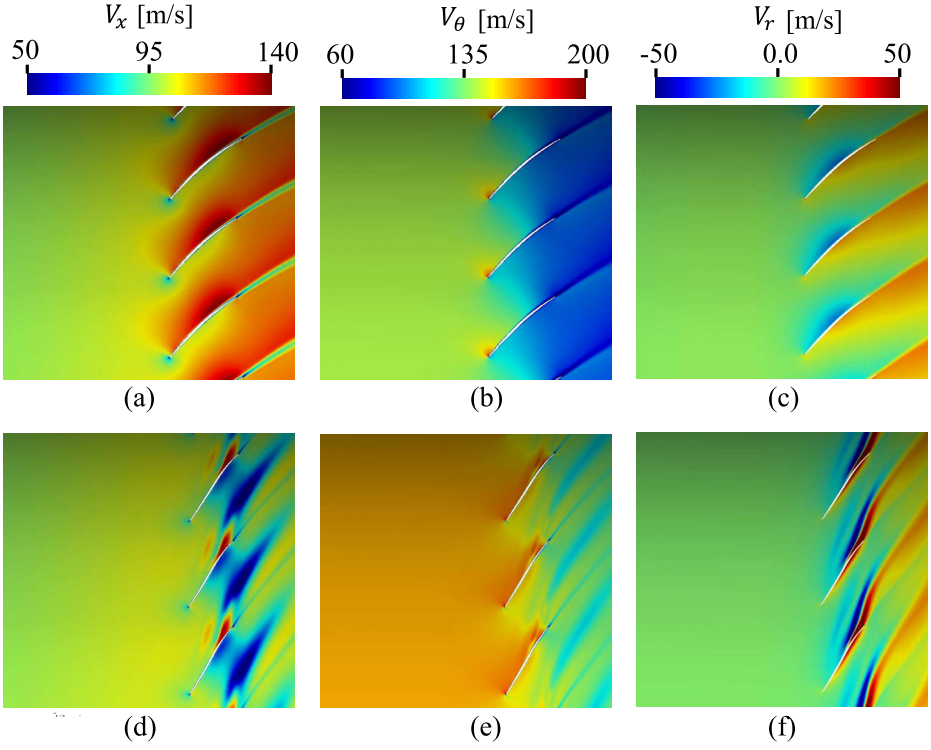

FIG. 9. Contours of the averaged velocity components around the rotor blades for two spanwise positions: (a), (b), and (c) 80% and (d), (e), and (f) 99%.

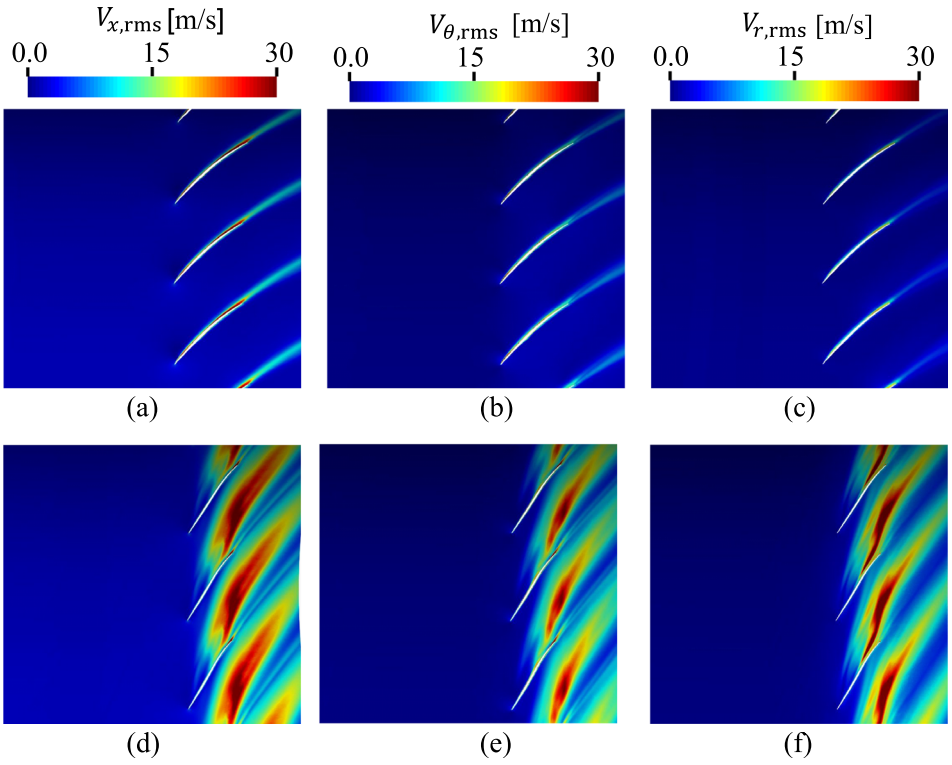

FIG. 10. Contours of the components of the RMS velocity fluctuations, around the rotor blade, at two spanwise positions: (a), (b), and (c) 80% and (d), (e), and (f) 99%.

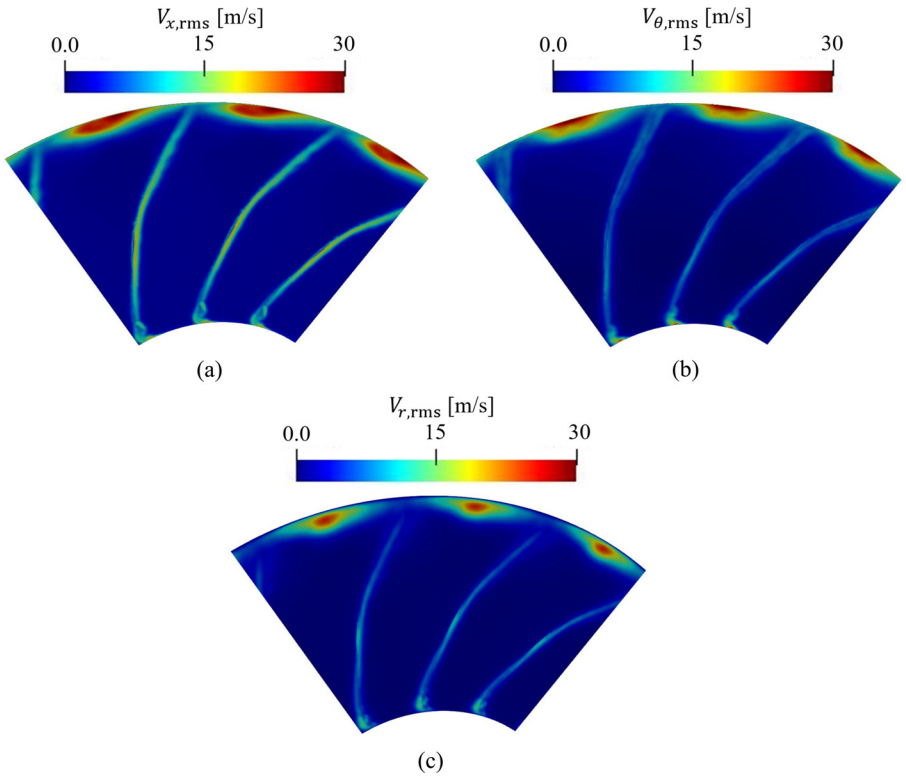

FIG. 11. Contours of the (a) axial, (b) circumferential, and (c) radial components of the RMS velocity fluctuations on an axial plane directly downstream of the rotor trailing edge.

observed in the tip-leakage region, which extend over 10% of the rotor span. It can also be noted that the velocity fluctuations in this region are higher than those in the wakes and in the corner separation region close to the hub. The tip-leakage flow is the dominant contributor to the velocity fluctuations.

Figure 12 presents the contours of the turbulent kinetic energy, k_t, and the loss in turbulent kinetic energy, LIKE, around the rotor blade at two spanwise positions. The LIKE parameter was first introduced by Daviller *et al.*,[36] and is defined as the sum of the dissipations associated with resolved and modeled fluctuations, i.e.,

$$\mathrm{LIKE} = (\mu + \mu_t)\left(\frac{\partial \tilde{V}_i}{\partial x_j} + \frac{\partial \tilde{V}_j}{\partial x_i}\right)^2, \tag{2}$$

where μ corresponds to the molecular viscosity, μ_t corresponds to the turbulent viscosity, and $\tilde{V}_i$ corresponds to the velocity component in the ith direction, which is filtered in the LES. The term $\mu(\frac{\partial V_i}{\partial x_j} + \frac{\partial V_j}{\partial x_i})^2$ is present in the transport equations of both the turbulent kinetic energy[37] and the entropy.[38] This term corresponds to the viscous dissipation in the equation of the turbulent kinetic energy and to the losses induced by the fluid friction irreversibilities in the entropy equation. Since LES does not resolve all spatial scales, LIKE is computed using the filtered velocity components for both the velocity fluctuations resolved by the LES $[\mu(\frac{\partial \tilde{V}_i}{\partial x_j} + \frac{\partial \tilde{V}_j}{\partial x_i})^2]$ and those modeled $[\mu_t(\frac{\partial \tilde{V}_i}{\partial x_j} + \frac{\partial \tilde{V}_j}{\partial x_i})^2]$.

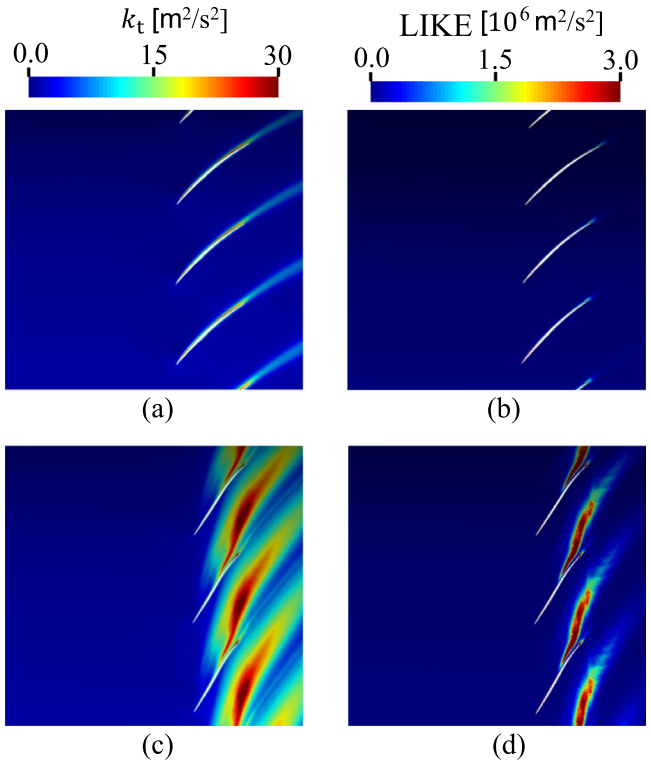

FIG. 12. Contours of (a) and (c) turbulent kinetic energy, (b) and (d) loss in turbulent kinetic energy,[36] and around the rotor blade, at two spanwise positions: (a) and (b) 80% and (c) and (d) 99%.

At the tip, the second tip-leakage vortex, TLV2, the induced vortex, IV, and the tip separation vortices, TSV, are the main contributors to k_t and LIKE. The loss in turbulent kinetic energy is localized at the core of the TLV2 and TSV and rapidly decreases downstream of the rotor.

The fan noise sources can be partly related to the RMS pressure fluctuations. Figure 13 presents the RMS pressure fluctuations, P_{rms}, around the rotor blade at two spanwise positions. At 80% of the rotor span, two regions of significant P_{rms} values are identified. The first region [labeled "1" in Fig. 13(a)] corresponds to the fluctuations in the recirculation bubble. This bubble appears close to the leading edge, on the suction side, between 60% and 90% of the rotor span, as shown in a previous study by the authors[26] using the same configuration and operating conditions. The second region [labeled "2" in Fig. 13(a)] corresponds to a small flow separation produced on the suction side, downstream of the maximum camber position. The influence of the tip vortices can be observed in Fig. 13(b). The first tip-leakage vortex TLV1 and the tip vortices TSV, TLV2, and IV can be identified in regions "3" and "4," respectively. The interaction between the TLV1 and the tip vortices TSV, TLV2, and IV is observed at region "5" in Fig. 13(b). High levels of P_{rms} are observed on the suction side between $0.7c_r$ and the trailing edge [region "6" in Fig. 13(b)]. This corresponds to the interaction of the TSV, TLV2, and IV with the blade surface in a detached flow region. Additionally, the TLV1 of each blade interacts with the trailing edge of the adjacent blade [region "7" in Fig. 13(b)], which generates large P_{rms} levels at the trailing edge on the pressure side. Thus, the main noise source is expected to be located at the trailing edge, due to these two interaction mechanisms: (i) the interaction between the TLV1 and the trailing edge of the adjacent blade [region 7 in Fig. 13(b)] and (ii) the interaction of the TSV, TLV2, and IV with the blade surface [region 6 in Fig. 13(b)]. These two noise mechanisms are confirmed by analyzing the coherence of the vortices in Sec. IV B. Furthermore, it can be noted that the size of the region with high pressure fluctuations is larger in the tip-gap region than that in the rotor wakes and in the recirculation bubble, which is consistent with the results in Figs. 10 and 11.

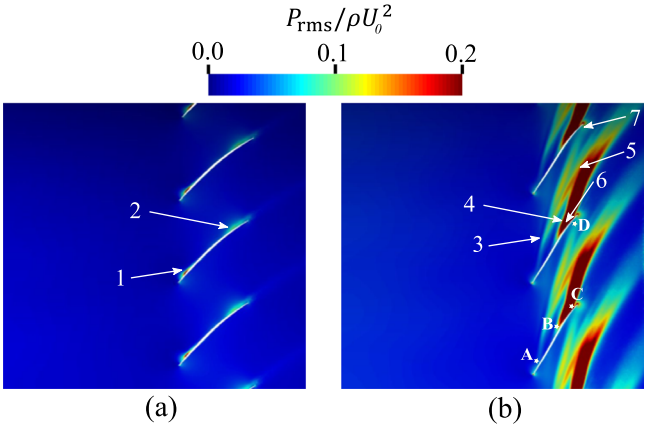

FIG. 13. Contours of RMS pressure fluctuations around the rotor blade, at two spanwise positions: (a) 80% and (b) 99%. The star symbols show the positions of the monitor points: A, B, C, and D, used for the computation of the coherence in the tip-gap region.

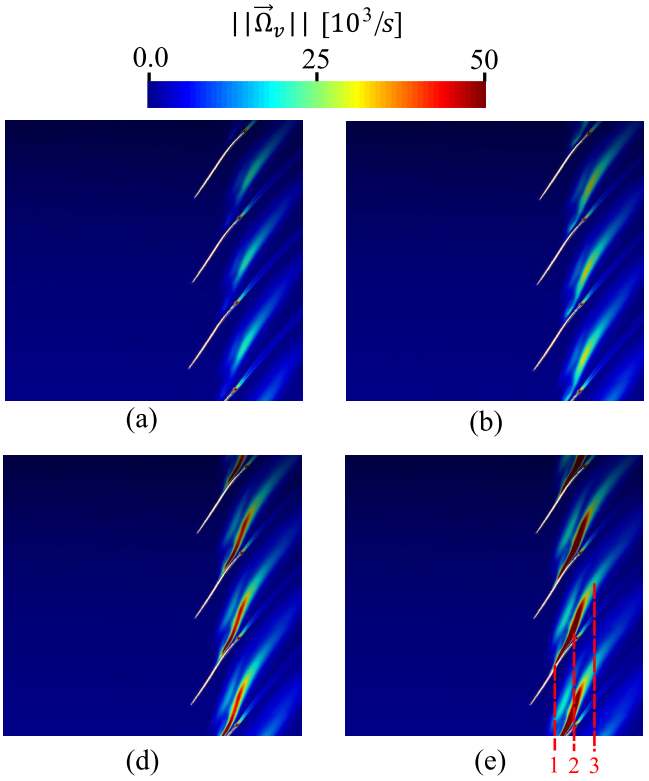

FIG. 14. Contours of the averaged vorticity magnitude around the rotor blade, at different spanwise positions: (a) 96%, (b) 97%, (c) 98%, and (d) 99%.

The tip-leakage vortex is often identified by a region of high vorticity magnitude. Figure 14 shows contour plots of the averaged vorticity magnitude at different spanwise positions, from 96% to 99% of the rotor span. At 99% of the rotor span, high vorticity values are observed close to the blade surface at about $0.7c_r$ [position 1 in Fig. 14(d)], which corresponds to the onset region of the tip flow vortices TSV, TLV2, and IV. The main core of these vortices is convected downstream with a changing direction. From position 1 to position 2, the TSV detaches from the blade tip due to the influence of the pressure difference. In this region, the TLV2 is not yet fully developed and TSV remains parallel to the blade chord. Between positions 2 and 3, the TLV2 is now fully formed and interacts with the TSV. Consequently, the tip vortices TSV and TLV2 deviate and form an angle of about 30 with respect to the blade chord. At position 3, these tip vortices are again deviated after interacting with both the main flow and the TLV1 and are convected in a direction parallel to the rotor wake. At lower radial positions, the maximum vorticity magnitude in the tip vortices is reduced and is shifted in the downstream direction, which shows the diffusion of the vortices.

The trajectory of the different tip vortices is further analyzed in Fig. 15 using averaged contours of the vorticity magnitude, the axial vorticity component, the turbulent kinetic energy, and the RMS pressure fluctuations, at several cross sections in a rotor passage. The cross sections are located at $0.2c_r$, $0.7c_r$, $0.9c_r$, and $1.2c_r$. All the tip flow vortical structures, which are already discussed in Sec. III, can be identified. At $0.2c_r$, the region of large k_t and P_{rms} values, close to the blade suction side (position 1 in Fig. 15), corresponds to the TLV1. The TLV1 can still be observed at $0.7c_r$, in the middle of the passage, with lower vorticity, k_t, and P_{rms} values. A small region (position 2 in Fig. 15) of large vorticity magnitude and P_{rms} highlights the interaction

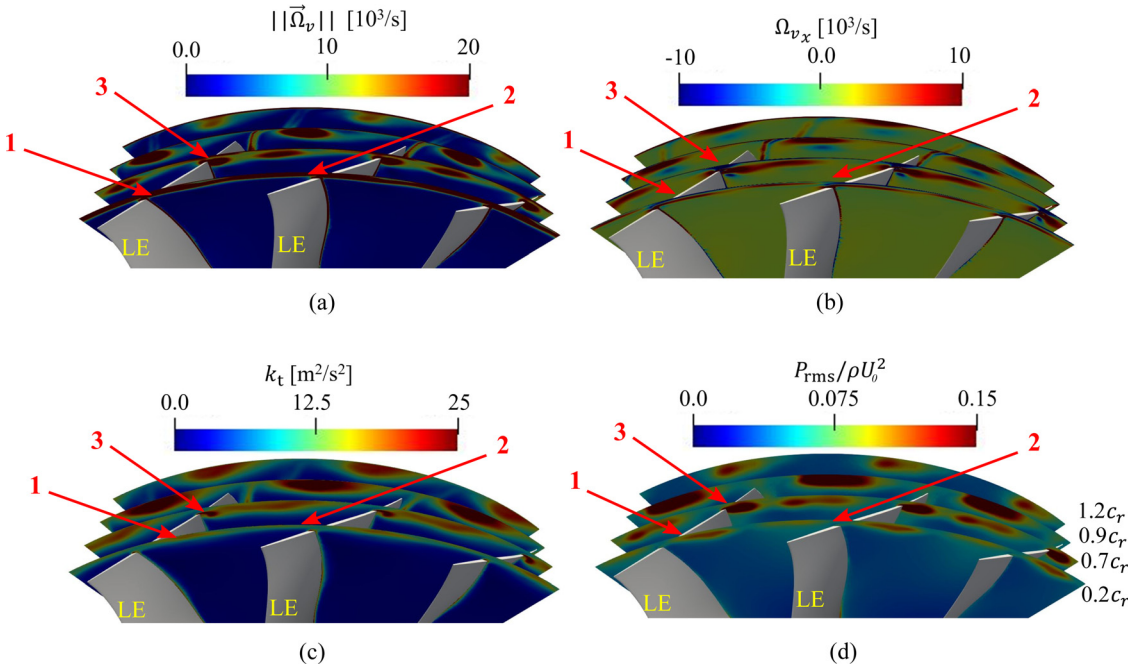

FIG. 15. Contours of averaged (a) vorticity magnitude, (b) axial vorticity component, (c) turbulent kinetic energy, and (d) RMS pressure fluctuations at four different axial cross sections in the blade passage. LE refers to the leading edge.

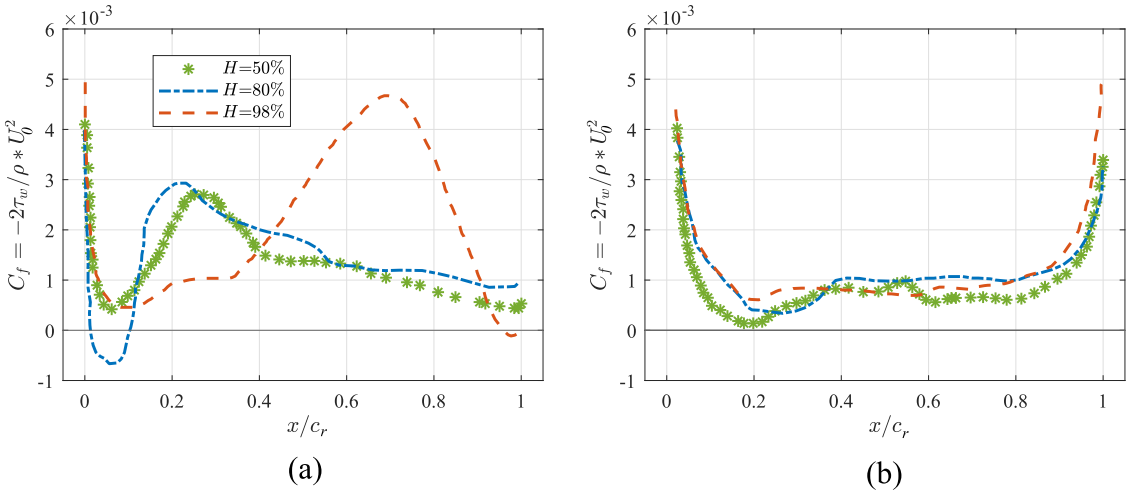

FIG. 16. Averaged friction coefficient, C_f, along the rotor blade at different spanwise positions: (a) suction side and (b) pressure side. τ_w is the skin shear stress.

of the HSV from the suction side of the adjacent blade with the pressure side of the current blade. At $0.7c_r$, the tip vortices TSV, TLV2, and IV appear close to the blade suction side (position 3 in Fig. 15). These vortices are convected downstream; the tip vortices TSV and TLV2 can be associated with positive values of the axial vorticity component, Ω_{v_x}, whereas IV can be associated with negative values of Ω_{v_x}.

A comparison of the friction coefficient, C_f, over the suction and pressure sides of the rotor blade is presented in Fig. 16, at different spanwise positions. For all the spanwise positions, positive values of C_f are observed on the pressure side, where the boundary layer remains attached. At 50% of the rotor span, C_f remains positive over the suction side. A region of negative friction coefficient is observed close to the leading edge of the blade at 80% of the rotor span, which is related to the presence of the recirculation bubble already mentioned. Downstream of this region, C_f remains positive along the suction side. At 98% of the rotor span, a slight increase in C_f is observed at about $0.2c_r$, which is followed by a region of high C_f between $0.5c_r$ and $0.85c_r$. This corresponds to the formation of the tip vortices TSV, TLV2, and IV at about $0.7c_r$ due to a high pressure jump between the pressure and suctions sides of the blade, as shown in Fig. 5.

IV. AEROACOUSTICS

A. Noise sources

Contours of instantaneous dilatation rate ($\nabla \cdot \mathbf{u}$) in a cross section that intersects the rotor blade are shown in Fig. 17, along with iso-surfaces of the Q-criterion ($Qc^2/U_0^2 = 100$) colored by the vorticity magnitude in the tip-gap region. In this figure, the flow is moving from left to right and only the suction side of the blades can be observed. The observer location is placed downstream of the fan. The flow topology in the tip-gap region and the different tip vortices, described in Sec. III, can be identified. Based on the wave-fronts that can be seen in the instantaneous contours of dilatation rate, an important noise source is present in the tip-gap region at approach conditions. The wave-fronts generated in the tip-gap region propagate in the upstream and downstream directions.

In order to further investigate (i) the turbulent structures in the tip-gap region and (ii) the relative contribution of the tip-gap noise when compared to the other fan noise sources, contours of the instantaneous dilatation rate ($\nabla \cdot \mathbf{u}$) at two spanwise positions are shown in Fig. 18 with iso-surfaces of Q-criterion. Contours of the Q-criterion are also shown in this figure, and the development of turbulent structures around the blades and in the wakes can be discussed.

At 80% of the rotor span, a small recirculation bubble appears near to the leading edge and triggers the transition of the boundary layer to turbulence. Small turbulent structures are thus formed on the suction side of the blade. These structures are diffracted at the trailing edge, which generates trailing edge noise. The contours of instantaneous dilatation rate show wave-fronts generated at the trailing edge and associated with the airfoil self-noise.

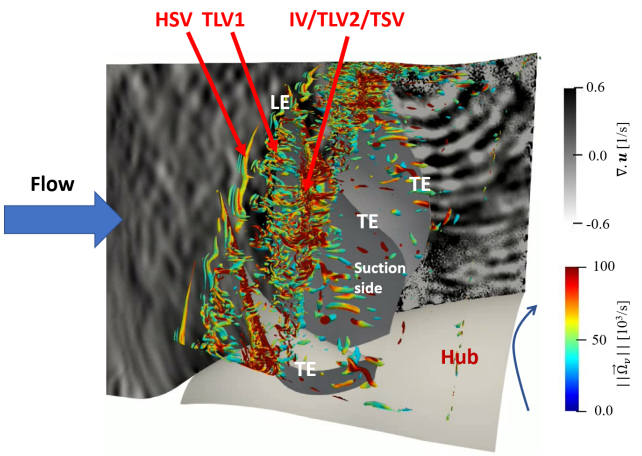

FIG. 17. Instantaneous contours of dilatation rate in a cross section that intersects the rotor blade and iso-surfaces of Q-criterion ($Qc_r^2/U_0^2 = 100$) colored by the vorticity magnitude in the tip-gap region. LE refers to the leading edge, and TE refers to the trailing edge.

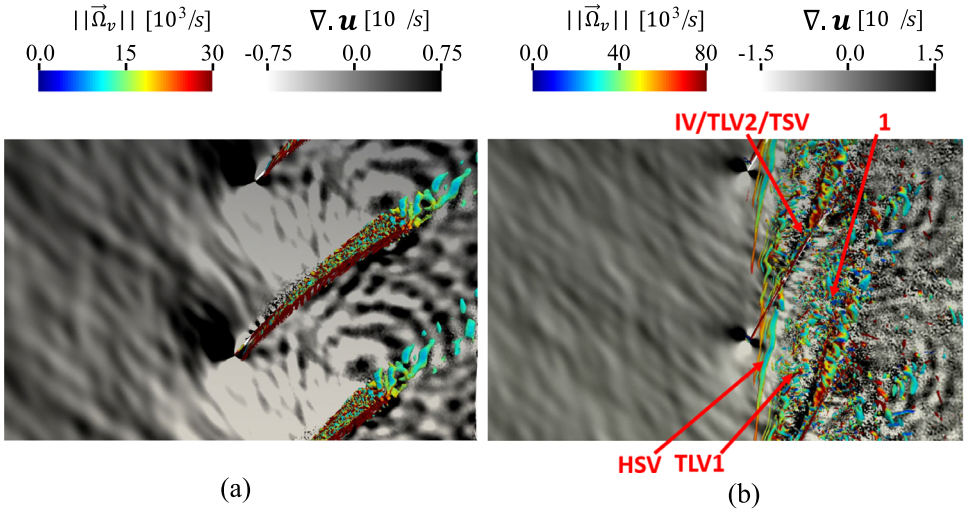

FIG. 18. Instantaneous contours of dilatation rate and iso-surfaces of Q-criterion ($Qc^2/U_0^2 = 100$) colored by the vorticity magnitude, around the rotor blades, at two spanwise positions: (a) 80% and (b) 98%.

At 98% of the rotor span, the different tip vortices (HSV, TLV1, TSV, TLV2, and IV) discussed in Sec. III are observed. The wavefronts identified using contours of instantaneous dilatation rate show that the main noise sources are located at the trailing edge. Two dipole noise mechanisms can be identified: (i) the interaction of the TLV1 from one blade with the trailing edge of the adjacent blade and (ii) the interaction of the tip vortices IV, TLV2, and TSV from each blade with its trailing edge. It should also be noted that the noise contribution due to the interaction between the different tip vortices, i.e., the quadrupolar noise sources from the interaction of TLV1 with TSV, TLV2, and IV in the rotor passage [position 1 in Fig. 18(b)], seems to be negligible when compared to the interaction of the tip vortices with the trailing edges.

When comparing the two spanwise positions, larger values of the dilatation rate are observed in the tip-gap region, which suggests that the dominant noise sources are related to the interaction of turbulent structures generated by the tip vortices with the trailing edges.

Larger P_{rms} levels can be associated with vortical structures convecting and interacting with the main flow, which leads to noise radiation of a quadrupolar nature. The P_{rms} levels can also be related to the interaction of vortical structures with the blade surface, particularly with the blade edges. The resulting unsteady loading on the blade produces noise of dipolar nature. Due to the relatively low Mach number in the present study, dipolar noise sources are expected to dominate.[39] Consequently, P_{rms} levels on the blade surface can be used to locate the dominant noise sources.[40] Figure 19 presents P_{rms} values along the rotor suction and pressure sides at different spanwise positions. At 50% of the rotor span, the small increase in P_{rms} at about $0.15c_r$ on the suction side indicates the position of the boundary layer transition to turbulence. The recirculation bubble, which appears at 80% of the

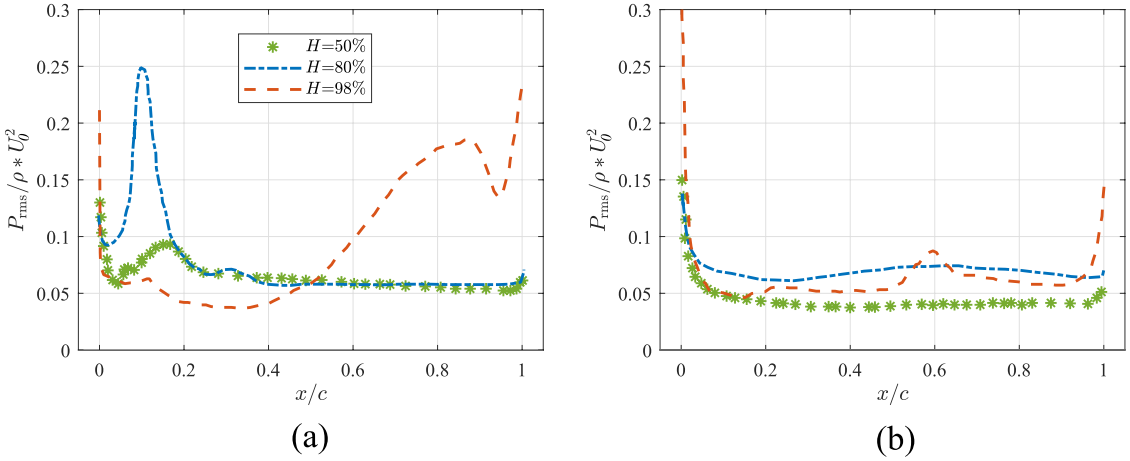

FIG. 19. RMS pressure fluctuations P_{rms} along the rotor blade, at different spanwise positions: (a) suction side and (b) pressure side.

rotor span close to the leading edge, also exhibits high P_{rms} values. In the tip region, a strong increase in P_{rms} is observed on the suction side from $0.6c_r$. This corresponds to the development of the tip vortices TLV2 and IV and the detachment of the TSV in a region with a high pressure difference between the pressure and suction sides of the blade. The impact of these vortices with the trailing edge leads to important P_{rms} values at this position, i.e., $x/c_r = 1$. On the pressure side, large values of P_{rms} are observed close to the trailing edge, due to the impact of the TLV1 from the adjacent blade. Since the tip vortices TSV, TLV2, and IV are characterized by larger vorticity magnitudes and turbulent intensities than TLV1, as shown in Figs. 12 and 14, the suction side exhibits larger P_{rms} levels than the pressure side at the trailing edge. Although the relation between the levels of P_{rms} and the intensity of the noise sources is not straightforward, it provides some information about the relative contribution of each noise source. Consequently, the dominant noise mechanism in the tip-gap region for the present configuration seems to be the interaction of the tip vortices TSV, TLV2, and IV, generated at about $0.7c_r$ with the trailing edge of the same blade.

Finally, a small hump in the P_{rms} distribution can be observed at the tip on the pressure side, from $0.5c_r$ to $0.7c_r$, which may be due to the interaction of some turbulent structures from the tip vortices HSV and TLV1 of the adjacent blade. This region also corresponds to the apparition of the tip vortices TSV, TLV2, and IV, which are probably influenced by this interaction.

B. Wall pressure spectra

The wall pressure spectrum (WPS) is a key indicator to describe the spectral content of the boundary layers and to characterize the airfoil self-noise sources.[3,41] The location of the monitor points on the suction side used to compute the WPS is presented in Fig. 20. The following nomenclature is used to refer to the different monitor points in Fig. 20. The value after "X" corresponds to the chordwise position of the monitor point, as a percentage of the chord length from the leading edge. The value after "H" corresponds to the spanwise position, as a percentage of the rotor span.

The WPS obtained using the four monitor points is also presented in Fig. 20. At 80% of the rotor span, similar WPS levels are observed for the probes at $0.2c_r$ and $0.98c_r$ up to 10 kHz, with a slope of about f^{-1} that corresponds to the large turbulent structures in the boundary layer. In this frequency range, self-similar non-dimensional spectra can be obtained for the WPS using internal and external variables of the boundary layer.[41] This region is known as the overlap region and is related to turbulent activity in the inertial logarithmic zone of the boundary layer.[41] The size of this region increases with the Reynolds number of the flow in the boundary layer. This slope has also been observed experimentally.[41] The monitor point at $0.2c_r$ is located in the recirculation bubble region, where large levels of RMS pressure fluctuations are observed in Fig. 19. This may explain the comparable levels of the WPS at this monitor point at the trailing edge, for which a highly turbulent boundary layer is expected.

The overlap region of the spectrum extends for the WPS close to the trailing edge up to approximately 40 kHz, whereas this region is limited to frequencies below 10 kHz at $0.2c_r$. This is due to a larger Reynolds number at $0.98c_r$.

At 98% of the rotor span, larger WPS levels are observed close to the trailing edge compared to the levels obtained at $0.2c_r$, over the whole frequency range, but particularly at high frequencies ($f > 10$ kHz). The overlap region extends from about 1.5 kHz up to 7 kHz for the WPS at $0.2c_r$, whereas it extends from 1.5 to 20 kHz at $0.98c_r$. After the overlap region, a hump is observed in the spectrum close to the trailing edge, which is probably associated with the tip flow.

In order to further investigate the pressure fluctuations in the tip-leakage region, several monitor points are located on the blade tip surface at different chordwise positions, including $0.3c_r$, $0.5c_r$, $0.7c_r$, and $0.9c_r$. The WPS at these positions is presented in Fig. 21.

Similar spectra are observed at $0.3c_r$ and $0.5c_r$, up to 12 kHz. For higher frequencies, the spectrum at $0.3c_r$ exhibits a plateau up to 40 kHz, whereas at $0.5c_r$, a significant hump is observed from 12 to 30 kHz. At $0.5c_r$, it is found that the TSV begins to separate from the blade and small turbulent structures are identified, as shown in Figs. 6 and 7. This hump is more pronounced at $0.7c_r$ and is identified from 9

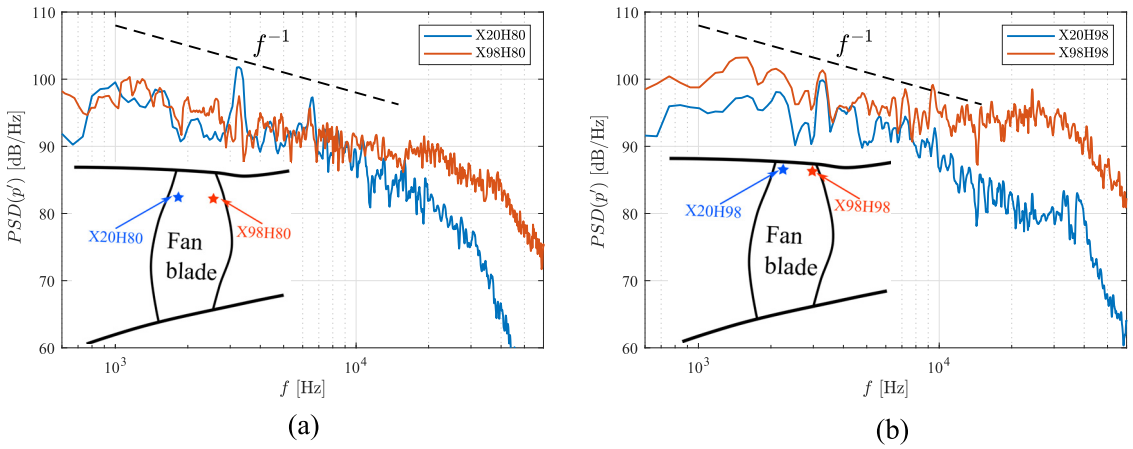

FIG. 20. WPS on the suction surface of the rotor blade, at several positions: (a) 80% and (b) 98% of the rotor span. p' corresponds to the pressure fluctuation. The reference pressure is $P_{ref} = 2 \times 10^{-5}$ Pa.

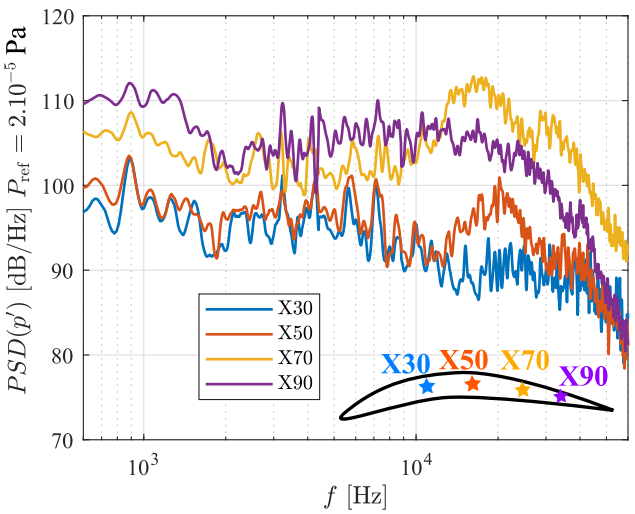

FIG. 21. WPS on the surface of the blade tip, at four different chordwise positions.

to 30 kHz. At this position, the pressure difference between the pressure and suction sides is significant, as shown in Fig. 5, and several tip vortices appear, including the TSV, TLV2, and IV, as shown in Figs. 6 and 7.

At $0.9c_r$, a hump in the WPS appears over a wide frequency range, from 2 kHz up to 30 kHz. At this position, two interaction mechanisms are identified: (i) the interaction of the TLV1 generated on the adjacent blade with the blade tip and (ii) the interaction of the tip vortices TSV, TLV2, and IV from the same blade. The high-frequency part of the hump observed at $0.9c_r$, between 9 and 30 kHz, can be attributed to the interaction mechanism of the tip vortices TSV, TLV2, and IV with the fan tip, as can be inferred from the spectra at $0.5c_r$ and $0.7c_r$. This will be further investigated in the following. From 2 to 9 kHz, the hump in the spectrum may be associated with the interaction between the TLV1 generated close to the leading edge of the adjacent blade and the blade tip. This hump is also observed in the literature in fan stages where the TLV1 is the dominant tip-leakage structure.[42,43] In the present study, the hump is centered around a Strouhal number (based on the tip clearance and the relative streamwise velocity at the tip) of $St = 0.0495$. This value is consistent with the study of Boudet *et al.*[42] on a fan stage, where a hump was identified around $St = 0.0576$, and is about twice higher than the Strouhal number, $St = 0.0248$, obtained in the cascade study of You *et al.*[43] When compared to tip-leakage studies using fixed profiles, the differences in the Strouhal number are more important. For instance, Lamidel *et al.*[13] have observed a hump at approximately $St = 0.185$.

Since the TLV1 travels through the whole blade passage before interacting with the trailing edge of the adjacent blade, it is wider than the tip vortices TSV, TLV2, and IV, when interacting with the blade surface. This may explain the lower frequency range induced by the interaction of the adjacent TLV1 with the blade, compared to the high frequency range associated with the interaction of the tip vortices TSV, TLV2, and IV with the same blade.

Due to the large range of turbulent coherent scales in the tip-leakage vortices, particularly at the position $0.9c_r$, the frequency range of the hump is relatively large.

To further analyze the different humps observed in the spectra, the coherence of the pressure fluctuations between different points in the tip-gap region is computed and presented in Fig. 22. Figure 13 presents the position of the monitor points used for the computation of the coherence. The monitor point A is close to the onset of the TLV1, and the monitor point "D" is located near the trailing edge on the pressure side. The coherence between these two positions corresponds to the mechanism of interaction of the TLV1 generated at one blade with the trailing edge of the adjacent blade on the pressure side. This coherence presents large values between 2 and 9 kHz, which is consistent with the analysis of Fig. 21 relating the hump at $0.9c_r$ from 2 to 9 kHz to the impact of the adjacent TLV1 with the pressure side.

The monitor point B is close to the detachment of the TSV and the onset of the tip vortices TLV2 and IV. The monitor point "C" is located near the trailing edge on the suction side. The coherence between these two positions (B and C) corresponds to the mechanism of interaction of the tip vortices TSV, TLV2, and IV with the trailing edge of the same blade on the suction side and presents large values between 9 and 30 kHz. This coherence study is also consistent with the

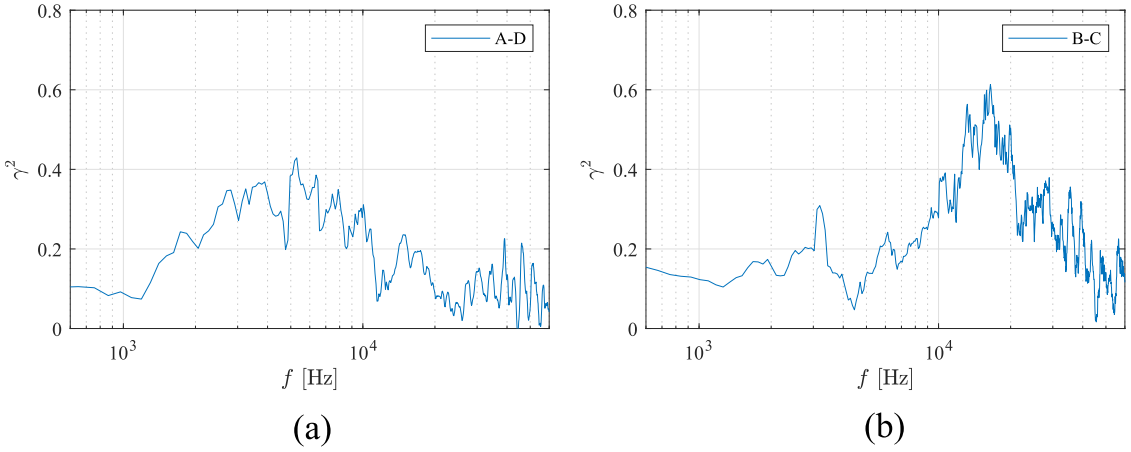

FIG. 22. Coherence between the pressure fluctuations at the monitor points A and D (a) and the monitor points B and C (b).

analysis of Fig. 21 regarding the origin of the high frequency part of the spectral hump, from 9 to 30 kHz, attributed to the interaction of the tip vortices TSV, TLV2, and IV with the suction side.

C. Dynamic mode tracking

The humps observed in Fig. 21 can be further investigated using a mode tracking technique, which is known as dynamic mode tracking (DMT).[44]

Figure 23 shows DMT results calculated from the density in the LES, at three different frequencies, $f_1 = 4000$ Hz, $f_2 = 6620$ Hz, and $f_3 = 16\,000$ Hz, using a frequency window width of 2000 Hz, on two axial cross sections upstream of the rotor blade, two spanwise positions (50% and 80% of the rotor span), and two longitudinal cross sections. The first longitudinal cross section (left column) is located close to the leading edge of the rotor, and the second cross section (right column) intersects the rotor blade at about $0.7c_r$. The first hump in the WPS spectra occurs in the f_1 and f_2 frequency ranges in Fig. 21, whereas the second hump occurs in the f_3 frequency range. Additionally, the f_2 frequency corresponds to the second harmonics of the vane passing frequency, as these analyses are performed in the rotor reference frame.

It should be noted that the mesh size and the numerical setup are able to properly resolve the acoustic waves up to three chord lengths upstream of the rotor blades, even at high frequency.

The dominant acoustic mode at $f_1 = 4000$ Hz exhibits large amplitudes close to the tip-gap region in the longitudinal cross section that is close to the leading edge [region A in Fig. 23(a)]. The amplitude of this mode increases from 50% of the rotor span to the blade tip. This mode propagates in the upstream direction with a decaying amplitude and with an inclination angle of about −50 with respect to the rotation axis, as shown by the dashed lines in Fig. 23(a).

At the second frequency ($f_2 = 6620$ Hz), a dominant acoustic mode seems to be generated downstream of the rotor blade and propagates in the upstream direction through the blade passage. This mode can be associated with the harmonics of the rotor–stator interaction

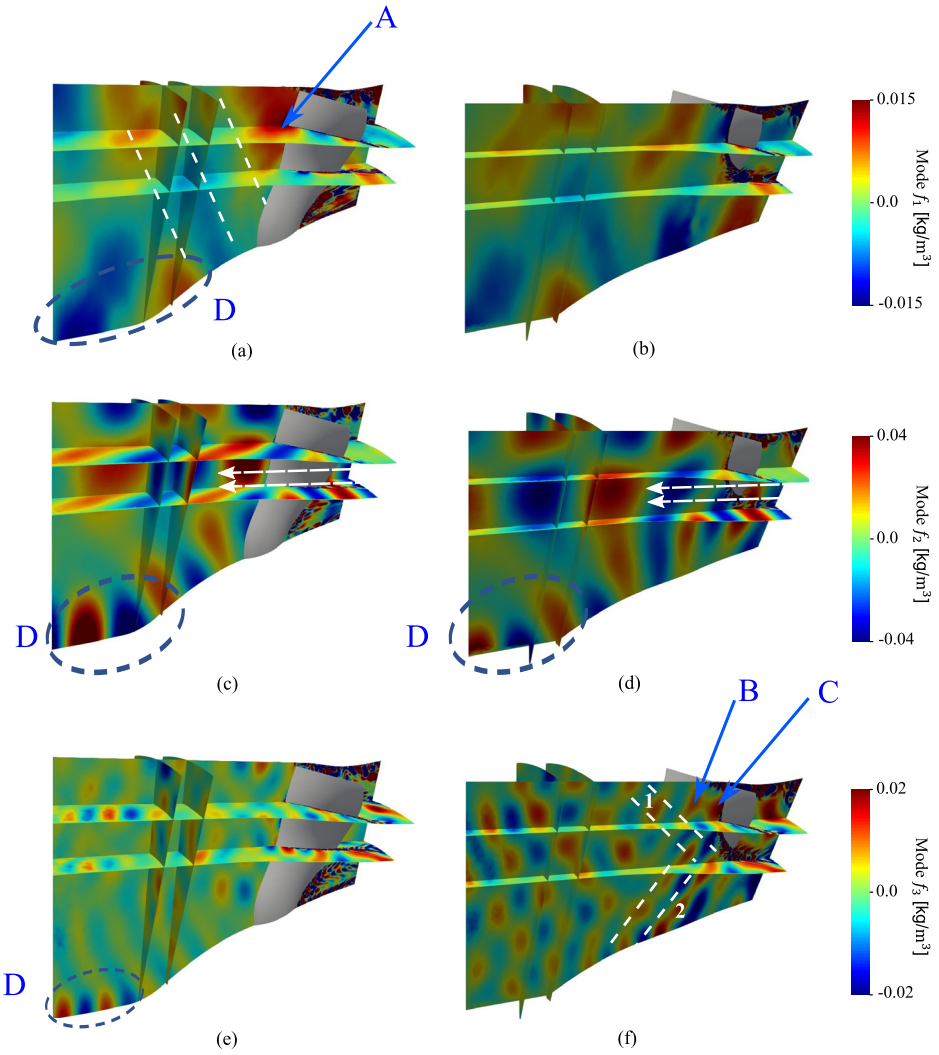

FIG. 23. Spatial distribution of the density modes using the DMT technique: (a) and (b) mode f_1; (c) and (d) mode f_2; and (e) and (f) mode f_3.

noise, which is related to the interaction between the periodic rotor wakes and the stator vanes. A similar behavior is observed on both longitudinal cross sections.

The DMT at $f_3 = 16\,000$ Hz exhibits a more complex directivity pattern. Two acoustic modes appear to be dominant, as it can be seen in the longitudinal cross section at $0.7c_r$ in Fig. 23(f). The first mode is generated from the lower part of the blade, close to the hub, and propagates in the upstream direction as shown by the dashed lines 2 in Fig. 23(f). The second mode is generated at the blade tip, with wave-fronts of large amplitudes observed. Two main lobes denoted as B and C in Fig. 23(f) can be seen. This mode also propagates in the upstream direction [dashed lines 1 in Fig. 23(f)], with a larger angle of inclination than the dominant mode at $f_1 = 4000$ Hz.

When analyzing the DMT results, the tip-leakage flow topology in Figs. 6 and 7, and the WPS in Fig. 21, it can be concluded that the DMT mode at f_1 is related to the TLV1, whereas the dominant mode at f_3 originating from the tip can be related to the tip vortices TSV, TLV2, and IV.

The amplitude of the different modes increases close to the hub in the region where the annular duct evolves toward a cylindrical duct in region D upstream of the spinner in Fig. 23. Due to the radius increase, some cutoff acoustic modes generated close to the fan become cut-on, which may explain the observed amplitude increase.

D. Tip-gap noise contributions

The far-field noise is predicted by the FWH analogy,[19] using the unsteady pressure fluctuations on the solid surface of the fan blade. The sampling frequency is set to 80 kHz, and the data are collected over four rotor revolutions. The advanced time approach of the formulation of Casalino[45] and Najafi-Yazd *et al.*[46] is adopted here. Only the fan blade surface is used for the computation of the dipolar term, since the main noise sources are located on both the pressure and suction sides, as found in Fig. 18. This is justified by the low Mach number flow, including in the tip-gap region. The acoustic propagation is computed using the free-field Green's function with a uniform flow. The monitor points are located on a sphere of radius 1.1 m, centered at the trailing edge of the tip blade airfoil. The far-field sound power level (SWL) spectrum is obtained using Welch's method[47] and Hann window with 50% overlap and a frequency resolution of $\Delta_f = 50$ Hz.

In order to estimate the influence of the tip-leakage flow on the far-field acoustic predictions, the blade is split into two parts. The upper 15% of the blade span is considered to compute the tip flow contribution to the far-field noise. The size of this region is chosen to be large enough to contain all the contributions of the blade tip vortices, as seen in Fig. 15, for instance. The lower 85% of the blade span is not significantly influenced by the tip flow. The total power spectral density of the far-field acoustic pressure from the full blade can be represented as the summation of power spectral density from each part of the blade [$(S_{pp})_{\text{tip}}$ and $(S_{pp})_{\text{low}}$] and the corresponding cross-spectral density [$(S_{pp})_{\text{cross}}$] as follows:

$$(S_{pp})_{\text{blade}} = (S_{pp})_{\text{tip}} + (S_{pp})_{\text{low}} + 2(S_{pp})_{\text{cross}}. \tag{3}$$

Figure 24 presents the SWL spectra in the upstream and downstream directions, with the above decomposition. For both the upstream and downstream directions, the cross correlation spectrum is relatively small compared to the other contributions, particularly at mid to high frequencies.

In the upstream direction, the noise sources in the lower part of the blade are dominant below 2 kHz. The difference between the lower part and the tip regions of the blade is about 10 dB in this frequency range. From 2 to 10 kHz, similar noise levels are observed from the different parts of the blade, whereas the SWL is larger at the blade tip from 10 to 20 kHz. In this frequency range, the difference in SWL between the tip and the lower parts is about 5 dB. Based on the coherence analysis from Fig. 22, the increase in the noise contribution of the tip region from 2 to 10 kHz is associated with the interaction of the TLV1 from a fan blade with the trailing edge of the adjacent blade. Additionally, the increase in the SWL for frequencies above 10 kHz is related to the noise source due to the interaction of the tip vortices TSV, TLV2, and IV with the trailing edge of the same blade.

In the downstream direction, the contribution of the lower part dominates the noise spectrum from 0.6 to 14 kHz. Up to 2 kHz, the difference in the noise levels between the lower and the tip parts is about 10 dB. This difference is reduced at higher frequencies. Similar

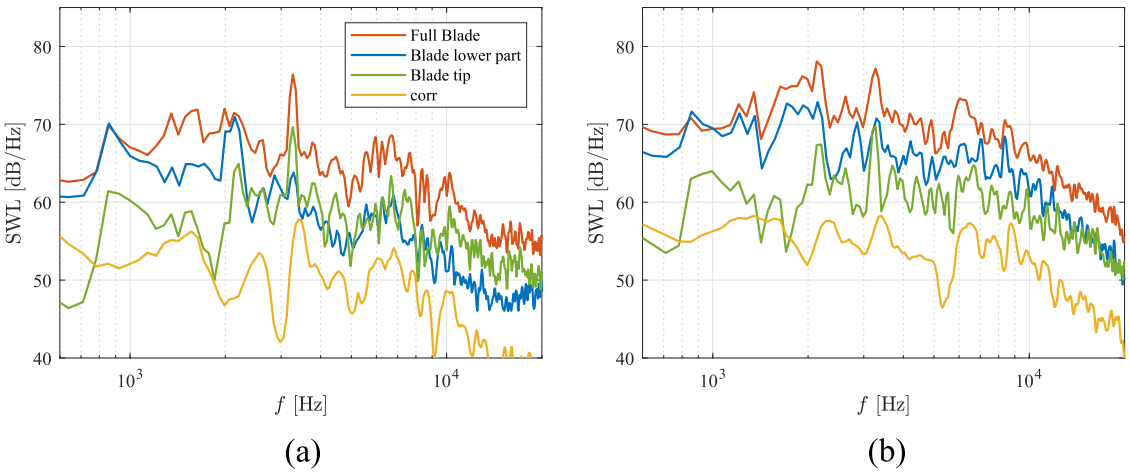

FIG. 24. SWL spectra from the FWH analogy[19] for the full blade (denoted "Full Blade"), the tip-gap region (denoted "Blade tip"), the lower part of the blade (denoted "Blade lower part"), and the cross correlation between them (denoted "corr"): (a) upstream direction and (b) downstream direction.

levels between the two parts are obtained at frequencies above 14 kHz. This behavior can also be explained by the two noise mechanisms at the tip region due to the interactions between the tip vortices and the blade trailing edges.

Consequently, it can be concluded that the main contribution of the tip-gap noise sources to the far-field noise can be perceived in the upstream direction at medium and high frequencies.

V. CONCLUSION

In the present paper, a wall-modeled LES has been performed on a scale model UHBR fan stage at approach conditions. A detailed analysis of the tip-leakage flow and the tip-gap noise has been presented. The LES mesh and numerical setup were chosen to ensure that the acoustic waves can be propagated to all monitor points in the frequency range of interest.

A complex flow is observed in the tip-gap region. Several tip vortices appear: (i) a horseshoe vortex (HSV) is present close to the leading edge of the blade, (ii) a first tip-leakage vortex (TLV1) is generated at about $0.25c_r$ from the leading edge, and (iii) a tip separation vortex (TSV) and a second tip-leakage vortex (TLV2), alongside with an induced vortex (IV), are formed at approximately $0.7c_r$. This last position corresponds to the region of large pressure difference between the two blade sides, which is observed on the isentropic Mach number. The tip vortices are characterized by strong spatial variations of the velocity components and large levels of turbulent kinetic energy. The helicity shows that the IV rotates in the opposite direction of the other tip vortices. The complex tip flow topology can be explained by the relatively large tip clearance at approach conditions and the blade section at the fan tip, which was designed to operate at transonic regime and has been investigated here in a subsonic flow.

The trajectories of the tip vortices TSV, TLV2, and IV have been analyzed by means of the vorticity magnitude. Three main directions are observed: (i) the first direction between $0.2c_r$ and $0.7c_r$ is parallel to the blade tip and corresponds to the evolution of the TSV, (ii) the second direction between $0.7c_r$ and $1.1c_r$ forms an angle of about 30 with the blade tip chord and corresponds to the interaction of the TSV with the TLV2 and IV, and (iii) the third direction beyond $1.1c_r$ seems to be parallel to the blade chord and corresponds to the interaction of the tip vortices TSV, TLV2, and IV with the TLV1 and the main flow. The vorticity magnitude of all fan tip vortices decreases rapidly with the distance in the downstream and radial directions.

Instantaneous contours of the dilatation rate and RMS pressure fluctuations have been analyzed to identify the location of the main noise sources. A significant noise source is observed in the tip-gap region at the trailing edge, which is associated with two noise mechanisms: (i) the interaction of the TLV1 from a fan blade with the trailing edge of the adjacent blade and (ii) the interaction of the tip vortices TSV, TLV2, and IV from a fan blade with its own trailing edge. The wall pressure spectra in the tip-gap region exhibit two main humps: the first hump extends from 2 to 9 kHz and the second one extends from 10 to 30 kHz. The formation of these spectral humps has been investigated using a coherence study between several monitor points in the tip-gap region and a dynamic mode tracking technique. Particularly, the first hump is related to the interaction of the TLV1 with the trailing edge of the adjacent blade, and the second hump is associated with the interaction of the tip vortices TSV, TLV2, and IV with the trailing edge of the same blade.

Finally, the acoustic far-field has been computed using the Ffowcs Williams and Hawkings analogy. To compare the contributions of the different noise sources to the far-field noise, the blade was split into two regions: the outer 15% of the blade, which corresponds to the blade tip, and the remaining part. This decomposition shows that the main contributions of the tip-gap noise occur in the frequency ranges of the humps in the wall pressure spectra. It also shows that the tip-gap noise becomes a significant noise source in the present configuration at medium to high frequencies (above 2 kHz) and in the upstream direction.

ACKNOWLEDGMENTS

This work was performed within the framework of the industrial chair ARENA (ANR-18-CHIN-0004-01) co-financed by Safran Aircraft Engines and the French National Research Agency (ANR) and is also supported by the Labex CeLyA of the Université de Lyon, operated by the French National Research Agency (ANR-11-LABX-0060/ANR-16-IDEX-0005).

The computational resources were provided by GENCI (CINES, Project No. A0102A05039), PRACE LESFAN (Project No. 2021240101), and FLMSN-PMCS2I at Ecole Centrale de Lyon.

Most of the post-processing was performed using Antares (release 1.16.0, https://www.cerfacs.fr/antares).

AUTHOR DECLARATIONS

Conflict of Interest

The authors have no conflicts to disclose.

Author Contributions

Jean Al Am: Conceptualization (lead); Data curation (lead); Formal analysis (lead); Funding acquisition (lead); Investigation (lead); Methodology (lead); Project administration (equal); Resources (equal); Software (equal); Validation (equal); Visualization (lead); Writing – original draft (lead); Writing – review & editing (equal). **Vincent Clair:** Conceptualization (equal); Formal analysis (equal); Investigation (equal); Project administration (equal); Supervision (equal); Writing – review & editing (equal). **Alexis Giauque:** Conceptualization (equal); Formal analysis (equal); Investigation (equal); Methodology (equal); Project administration (equal); Resources (equal); Software (equal); Supervision (equal); Writing – review & editing (equal). **Jérôme Boudet:** Conceptualization (equal); Formal analysis (equal); Investigation (equal); Methodology (equal); Project administration (equal); Resources (equal); Supervision (equal); Writing – review & editing (equal). **Fernando Gea-Aguilera:** Conceptualization (equal); Formal analysis (equal); Investigation (equal); Project administration (equal); Supervision (equal); Writing – review & editing (equal).

DATA AVAILABILITY

The data that support the findings of this study are available from the corresponding author upon reasonable request.

REFERENCES

[1]S. Moreau, "Turbomachinery noise predictions: Present and future," Acoustics **1**, 92–116 (2019).

[2]S. Moreau, "A review of turbomachinery noise: From analytical models to high-fidelity simulations," in *Fundamentals High Lift Future Civil Aircraft* (Springer, Cham, 2021), pp. 579–595.
[3]M. Roger and S. Moreau, "Back-scattering correction and further extensions of Amiet's trailing-edge noise model. Part 1: Theory," J. Sound Vib. **286**, 477–506 (2005).
[4]J. Al-Am, V. Clair, A. Giauque, J. Boudet, and F. Gea-Aguilera, "On the effects of a separation bubble on fan noise," J. Sound Vib. **537**, 117180 (2022).
[5]D. A. Rains, "Tip clearance flows in axial compressors and pumps," Ph.D. thesis (California Institute of Technology, 1954).
[6]D. You, M. Wang, P. Moin, and R. Mittal, "Large-eddy simulation analysis of mechanisms for viscous losses in a turbomachinery tip-clearance flow," J. Fluid Mech. **586**, 177–204 (2007).
[7]P. Kholodov and S. Moreau, "Identification of noise sources in a realistic turbofan rotor using large eddy simulation," Acoustics **2**, 691–706 (2020).
[8]F. Kameier and W. Neise, "Experimental study of tip clearance losses and noise in axial turbomachines and their reduction," J. Turbomach. **119**, 460–471 (1997).
[9]J. Grilliat, M. Jacob, R. Camussi, and G. Caputi-Gennaro, "Tip leakage experiment-part one: Aerodynamic and acoustic measurements," AIAA Paper No. 2007-3684, 2007.
[10]M. C. Jacob, E. Jondeau, and B. Li, "Time-resolved PIV measurements of a tip leakage flow," Int. J. Aeroacoust. **15**, 662–685 (2016).
[11]J. Boudet, J. Caro, B. Li, E. Jondeau, and M. C. Jacob, "Zonal large-eddy simulation of a tip leakage flow," Int. J. Aeroacoust. **15**, 646–661 (2016).
[12]T. Zhu, D. Lallier-Daniels, M. Sanjosé, S. Moreau, and T. Carolus, "Rotating coherent flow structures as a source for narrowband tip clearance noise from axial fans," J. Sound Vib. **417**, 198–215 (2018).
[13]D. Lamidel, G. Daviller, M. Roger, and H. Posson, "Numerical prediction of the aerodynamics and acoustics of a tip leakage flow using large-eddy simulation," Int. J. Turbomach., Propul. Power **6**, 27 (2021).
[14]R. Koch, M. Sanjosé, and S. Moreau, "Large-eddy simulation of a single airfoil tip-leakage flow," AIAA J. **59**, 2546–2557 (2021).
[15]A. Mann, M.-S. Kim, J. Wu, F. Pérot, J. Grilliat, M. C. Jacob, and M. Colman, "Airfoil tip leakage aeroacoustics predictions using a lattice Boltzmann based method," AIAA Paper No. 2016-2825, 2016.
[16]S. Kang and C. Hirsch, "Tip leakage flow in linear compressor cascade," J. Turbomach. **116**, 657–664 (1994).
[17]R. Koch, M. Sanjosé, and S. Moreau, "Aerodynamic investigation of a linear cascade with tip gap using large-eddy simulation," J. Global Power Propul. Soc. **5**, 39–49 (2021).
[18]R. Koch, M. Sanjosé, and S. Moreau, "Large-eddy simulation of a linear compressor cascade with tip gap: Aerodynamic and acoustic analysis," AIAA Paper No. 2021-2312, 2021.
[19]J. F. Williams and L. Hall, "Aerodynamic sound generation by turbulent flow in the vicinity of a scattering half plane," J. Fluid Mech. **40**, 657–670 (1970).
[20]E. Canepa, A. Cattanei, F. Mazzocut Zecchin, G. Milanese, and D. Parodi, "An experimental investigation on the tip leakage noise in axial-flow fans with rotating shroud," J. Sound Vib. **375**, 115–131 (2016).
[21]H. Lee, K. Park, and H. Choi, "Experimental investigation of tip-leakage flow in an axial flow fan at various flow rates," J. Mech. Sci. Technol. **33**, 1271–1278 (2019).
[22]C. Pérez Arroyo, T. Leonard, M. Sanjosé, S. Moreau, and F. Duchaine, "Large eddy simulation of a scale-model turbofan for fan noise source diagnostic," J. Sound Vib. **445**, 64–76 (2019).
[23]P. Kholodov, M. Sanjose, and S. Moreau, "Tip flow evolution in a turbofan rotor for broadband noise diagnostic," AIAA Paper No. 2020-2521, 2020.
[24]V. Pagès, P. Duquesne, S. Aubert, L. Blanc, P. Ferrand, X. Ottavy, and C. Brandstetter, "UHBR open-test-case fan ECL5/CATANA," Int. J. Turbomach., Propul. Power **7**, 17 (2022).
[25]M. M. Rai and N. K. Madavan, "Multi-airfoil Navier–Stokes simulations of turbine rotor–stator interaction," J. Turbomach. **112**, 377–384 (1990).
[26]J. Al-Am, V. Clair, A. Giauque, J. Boudet, and F. Gea-Aguilera, "Direct noise predictions of fan broadband noise using LES and analytical models," AIAA Paper No. 2022-2882, 2022.
[27]T. Schonfeld and M. Rudgyard, "Steady and unsteady flow simulations using the hybrid flow solver AVBP," AIAA J. **37**, 1378–1385 (1999).
[28]G. Wang, F. Duchaine, D. Papadogiannis, I. Duran, S. Moreau, and L. Y. Gicquel, "An overset grid method for large eddy simulation of turbomachinery stages," J. Comput. Phys. **274**, 333–355 (2014).
[29]O. Colin and M. Rudgyard, "Development of high-order Taylor-Galerkin schemes for LES," J. Comput. Phys. **162**, 338–371 (2000).
[30]F. Nicoud, H. B. Toda, O. Cabrit, S. Bose, and J. Lee, "Using singular values to build a subgrid-scale model for large eddy simulations," Phys. Fluids **23**, 085106 (2011).
[31]T. Poinsot and S. Lele, "Boundary conditions for direct simulations of compressible viscous flows," J. Comput. Phys. **101**, 104–129 (1992).
[32]P. Schmitt, T. Poinsot, B. Schuermans, and K. P. Geigle, "Large-eddy simulation and experimental study of heat transfer, nitric oxide emissions and combustion instability in a swirled turbulent high-pressure burner," J. Fluid Mech. **570**, 17–46 (2007).
[33]J. Boudet, J.-F. Monier, and F. Gao, "Implementation of a roughness element to trip transition in large-eddy simulation," J. Therm. Sci. **24**, 30–36 (2015).
[34]J. Al-Am, V. Clair, A. Giauque, J. Boudet, and F. Gea-Aguilera, "A parametric study on the LES numerical setup to investigate fan/OGV broadband noise," Int. J. Turbomach., Propul. Power **6**, 12 (2021).
[35]T. J. Praisner and C. R. Smith, "The dynamics of the horseshoe vortex and associated endwall heat transfer—Part I: Temporal behavior," J. Turbomach. **128**, 747–754 (2005).
[36]G. Daviller, M. Brebion, P. Xavier, G. Staffelbach, J.-D. Müller, and T. Poinsot, "A mesh adaptation strategy to predict pressure losses in LES of swirled flows," Flow, Turbul. Combust. **99**, 93–118 (2017).
[37]G. Wang, F. Yang, K. Wu, Y. Ma, C. Peng, T. Liu, and L.-P. Wang, "Estimation of the dissipation rate of turbulent kinetic energy: A review," Chem. Eng. Sci. **229**, 116133 (2021).
[38]D. M. McEligot, E. J. Walsh, E. Laurien, and P. R. Spalart, "Entropy generation in the viscous parts of turbulent boundary layers," J. Fluids Eng. **130**, 061205 (2008).
[39]D. Hanson and M. Fink, "The importance of quadrupole sources in prediction of transonic tip speed propeller noise," J. Sound Vib. **62**, 19–38 (1979).
[40]M. Roger, S. Moreau, and K. Kucukcoskun, "On sound scattering by rigid edges and wedges in a flow, with applications to high-lift device aeroacoustics," J. Sound Vib. **362**, 252–275 (2016).
[41]Y. Rozenberg, G. Robert, and S. Moreau, "Wall-pressure spectral model including the adverse pressure gradient effects," AIAA J. **50**, 2168–2179 (2012).
[42]J. Boudet, A. Cahuzac, P. Kausche, and M. C. Jacob, "Zonal large-eddy simulation of a fan tip-clearance flow, with evidence of vortex wandering," J. Turbomach. **137**, 061001 (2015).
[43]D. You, M. Wang, P. Moin, and R. Mittal, "Vortex dynamics and low-pressure fluctuations in the tip-clearance flow," J. Fluids Eng. **129**, 1002–1014 (2007).
[44]M. Queguineur, L. Gicquel, F. Dupuy, A. Misdariis, and G. Staffelbach, "Dynamic mode tracking and control with a relaxation method," Phys. Fluids **31**, 034101 (2019).
[45]D. Casalino, "An advanced time approach for acoustic analogy predictions," J. Sound Vib. **261**, 583–612 (2003).
[46]A. Najafi-Yazdi, G. A. Brès, and L. Mongeau, "An acoustic analogy formulation for moving sources in uniformly moving media," Proc. R. Soc. A **467**, 144–165 (2011).
[47]P. Welch, "The use of fast Fourier transform for the estimation of power spectra: A method based on time averaging over short, modified periodograms," IEEE Trans. Audio Electroacoust. **15**, 70–73 (1967).